



|                               |   |
|-------------------------------|---|
| <b>Publication Year</b>       | 2019  |
| <b>Acceptance in OA @INAF</b> | 2021-01-21T19:10:33Z  |
| <b>Title</b>                  | The evolution of CNO isotopes: the impact of massive stellar rotators                           |
| <b>Authors</b>                | ROMANO, Donatella; Matteucci, Maria Francesca; Zhang, Zhi-Yu; Ivison, Rob J.; VENTURA, Paolo    |
| <b>DOI</b>                    | 10.1093/mnras/stz2741   |
| <b>Handle</b>                 | <a href="http://hdl.handle.net/20.500.12386/29936">http://hdl.handle.net/20.500.12386/29936</a> |
| <b>Journal</b>                | MONTHLY NOTICES OF THE ROYAL ASTRONOMICAL SOCIETY   |
| <b>Number</b>                 | 490   |

# The evolution of CNO isotopes: the impact of massive stellar rotators

Donatella Romano,<sup>1</sup><sup>\*</sup> Francesca Matteucci,<sup>2,3,4</sup> Zhi-Yu Zhang,<sup>5,6</sup> Rob J. Ivison<sup>5,6</sup>  
and Paolo Ventura<sup>7</sup>

<sup>1</sup> *INAF, Osservatorio di Astrofisica e Scienza dello Spazio, Via Gobetti 93/3, I-40129 Bologna, Italy*

<sup>2</sup> *Dipartimento di Fisica, Sezione di Astronomia, Università di Trieste, Via Tiepolo 11, I-34131 Trieste, Italy*

<sup>3</sup> *INAF, Osservatorio Astronomico di Trieste, Via Tiepolo 11, I-34131 Trieste, Italy*

<sup>4</sup> *INFN, Sezione di Trieste, Via Valerio 2, I-34127 Trieste, Italy*

<sup>5</sup> *Institute for Astronomy, University of Edinburgh, Royal Observatory, Blackford Hill, Edinburgh, EH9 3HJ, UK*

<sup>6</sup> *European Southern Observatory, Karl-Schwarzschild-Strasse 2, D-85748, Garching bei München, Germany*

<sup>7</sup> *INAF, Osservatorio Astronomico di Roma, Via Frascati 33, I-00040 Monte Porzio Catone, Roma, Italy*

Accepted . Received ; in original form 2019 July 19

## ABSTRACT

Chemical abundances and abundance ratios measured in galaxies provide precious information about the mechanisms, modes and time scales of the assembly of cosmic structures. Yet, the nucleogenesis and chemical evolution of elements heavier than helium are dictated mostly by the physics of the stars and the shape of the stellar mass spectrum. In particular, estimates of CNO isotopic abundances in the hot, dusty media of high-redshift starburst galaxies offer a unique glimpse into the shape of the stellar initial mass function (IMF) in extreme environments that can not be accessed with direct observations (star counts). Underlying uncertainties in stellar evolution and nucleosynthesis theory, however, may hurt our chances of getting a firm grasp of the IMF in these galaxies. In this work, we adopt new yields for massive stars, covering different initial rotational velocities. First, we implement the new yield set in a well-tested chemical evolution model for the Milky Way. The calibrated model is then adapted to the specific case of a prototype submillimeter galaxy (SMG). We show that, if the formation of fast-rotating stars is favoured in the turbulent medium of violently star-forming galaxies irrespective of metallicity, the IMF needs to be skewed towards high-mass stars in order to explain the CNO isotope ratios observed in SMGs. If, instead, stellar rotation becomes negligible beyond a given metallicity threshold, as is the case for our own Galaxy, there is no need to invoke a top-heavy IMF in starbursts.

**Key words:** nuclear reactions, nucleosynthesis, abundances – galaxies: abundances – galaxies: evolution – galaxies: ISM – stars: abundances – stars: rotation.

## 1 INTRODUCTION

After hydrogen and helium, oxygen, carbon and nitrogen are the most abundant elements in the universe. Their seven stable isotopes,  $^{12}\text{C}$ ,  $^{13}\text{C}$ ,  $^{14}\text{N}$ ,  $^{15}\text{N}$ ,  $^{16}\text{O}$ ,  $^{17}\text{O}$ , and  $^{18}\text{O}$ , are synthesised in different stellar sites through different processes (Burbidge et al. 1957): (i) the main isotopes of carbon and oxygen come from He burning in stars of all masses ( $^{12}\text{C}$ ) or in massive stars only ( $^{16}\text{O}$ ); (ii) the cold CNO cycle, that takes place in the H-burning zones of main sequence and giant branch stars in the presence of carbon- (and oxygen-)seed nuclei, leads to the production of  $^{14}\text{N}$  and, possibly,  $^{13}\text{C}$  and  $^{17}\text{O}$  (at a lower pace); (iii) in the external layers of novae and supernovae (SNe), the activation of the hot CNO cycle explains the formation of  $^{13}\text{C}$ ,  $^{15}\text{N}$ , and  $^{17}\text{O}$  in H-rich zones, and (iv) of  $^{15}\text{N}$  and  $^{18}\text{O}$  in He-rich ones.

While  $^{12}\text{C}$  and  $^{16}\text{O}$  are purely primary elements, i.e., they form directly from a hydrogen-helium mixture through a succession of nuclear burnings, all other isotopes may have a primary and/or secondary nature, depending on whether the metal seeds necessary for their formation are produced inside the star, or are already present on the zero-age main sequence. Whether it is the primary contribution or the secondary one that prevails, it depends primarily on the initial mass and metallicity of the star. For instance, fast-rotating intermediate- and high-mass stars produce large amounts of primary  $^{14}\text{N}$  at very low metallicities, via production channels that lose their effectiveness at higher metallicities (Meynet & Maeder 2002). This primary N production was hypothesised long ago (Truran & Cameron 1971; Talbot & Arnett 1974) and explains observations of  $[\text{N}/\text{O}]$ <sup>1</sup> abundance ratios in metal-

<sup>\*</sup> E-mail: donatella.romano@inaf.it

<sup>1</sup> In this paper, we adopt standard definitions of elemental abundance ratios. For two elements X and Y,  $[\text{X}/\text{Y}] \equiv \log(N_{\text{X}}/N_{\text{Y}}) - \log(N_{\text{X}}/N_{\text{Y}})_{\odot}$  is the ratio

poor Galactic dwarfs and ionized HII regions in our own and other galaxies (see [Snedden 1974](#); [Smith 1975](#); [Edmunds & Pagel 1978](#); [Peimbert et al. 1978](#); [Lequeux et al. 1979](#); [Barbuy 1983](#); [Matteucci & Tosi 1985](#), for early work pointing to the need for some primary N production at low metallicities).

In chemical evolution studies, it is customary to use abundance ratios to gain insights into the mechanisms that shape galaxies, and their time scales. As matter is more and more strongly processed by succeeding generations of stars, one might naively expect an increase in the abundances of secondary elements relative to those of primary elements. However, elements that are produced via primary nucleosynthetic processes in low-mass stars will behave as secondary elements from the point of view of chemical evolution, owing to the long lifetimes of their progenitors (e.g. [Matteucci & François 1989](#)); similarly, primary elements originating in the outer layers of massive stars may exhibit a pseudo-secondary character, if their production is boosted at higher metallicities because of enhanced mass loss ([Maeder 1992](#); [Henry et al. 2000](#)).

With their multifaceted stellar production sites and nucleosynthesis paths, CNO isotopes have repeatedly attracted the attention of chemical evolution modelers. Following pioneering works by [Audouze et al. \(1975; 1977\)](#), [Vigroux et al. \(1976\)](#) and [Dearborn et al. \(1978\)](#), many authors have attempted to explain the origin and evolution of (one or more) CNO isotope ratios in the framework of increasingly sophisticated models. These, however, have mostly dealt with the Milky Way (e.g. [Tosi 1982](#); [Matteucci & D’Antona 1991](#); [Prantzos et al. 1996](#); [Romano & Matteucci 2003](#); [Chiappini et al. 2008](#); [Kobayashi et al. 2011](#)), with a few exceptions ([Henkel & Mauersberger 1993](#); [Hughes et al. 2008](#); [Romano et al. 2017](#)).

Nowadays, although important uncertainties remain, the constant improvement of stellar evolution and nucleosynthesis theory on the one hand, and the advent of revolutionary instrumentation of unprecedented sensitivity on the other, allow an effective usage of specific CNO isotope ratios as sensible constraints on general models of galaxy formation and evolution. In [Romano et al. \(2017\)](#), we have extended a successful Galactic chemical evolution (GCE) model, that reproduces satisfactorily well the CNO abundance data for the Milky Way, to other galaxies and shown that the predicted  $^{16}\text{O}/^{18}\text{O}$  abundance ratio may decrease by orders of magnitude if the assumed stellar initial mass function (IMF) in galaxy-wide starbursts varies from a canonical to a top-heavy one; the same IMF changes have only a minor effect on the  $^{12}\text{C}/^{13}\text{C}$  ratio<sup>2</sup>. Building on this, in [Zhang et al. \(2018\)](#) we read the remarkably uniform  $^{13}\text{C}/^{18}\text{O} \approx 1$  ratio measured by us in four strongly lensed submillimeter galaxies (SMGs) observed with the Atacama Large Millimeter/submillimeter Array (ALMA) at redshift  $z \sim 2\text{--}3$  as a clear-cut evidence that the IMF is biased towards massive stars in the most extreme starburst events in the universe, and propose to use this ratio as a powerful diagnostic of the IMF shape in dust-enshrouded galaxies.

Several independent, more or less direct pieces of observational evidence ([Nayakshin & Sunyaev 2005](#); [Bradford et al. 2009](#); [Gunawardhana et al. 2011](#); [Lu et al. 2013](#); [Schneider et al. 2018](#)), as well as theoretical arguments (see [Alexander et al. 2008](#);

[Papadopoulos 2010](#); [Papadopoulos et al. 2011](#); [Jeřábková et al. 2018](#), among others), support our finding that massive star formation is favoured in extreme environments, such as dense star-forming regions of high temperature and pressure permeated by intense radiation fields. However, new grids of stellar yields have been published recently ([Limongi & Chieffi 2018](#)), which might challenge our interpretation of the low  $^{13}\text{C}/^{18}\text{O}$  ratios observed in SMGs. Indeed, even small differences in the yields, when weighted by an appropriate IMF, may result in non-negligible effects on galactic-scale model predictions (e.g. [Romano et al. 2010](#)). Therefore, a reappraisal of our models in the light of the newly published nucleosynthesis results is urgently needed.

This paper is organized as follows: in Section 2, we briefly outline the main assumptions and ingredients of our chemical evolution models, with special emphasis on the adopted nucleosynthesis prescriptions. In Section 3, we present the model results in comparison to up-to-date data for the Milky Way and for the SMGs studied by [Zhang et al. \(2018\)](#). We discuss our findings in Section 4; the conclusions follow (Section 5).

## 2 CHEMICAL EVOLUTION MODELS

### 2.1 The Milky Way model

As in [Romano et al. \(2017\)](#), we adopt the two-infall chemical evolution model for the Milky Way originally developed by [Chiappini et al. \(1997, 2001\)](#), where a detailed description of the basic equations and assumptions can be found. In the next paragraphs, we briefly summarize its main features, strengths, and limitations.

The model embraces a multi-zone scheme and divides the Galactic disc in several concentric annuli 2 kpc wide. It assumes that the inner halo and thick-disc components form out of a first episode of accretion of matter of primordial chemical composition. In the first  $\sim 1$  Gyr of evolution, the fast gas consumption resulting from the efficient star formation burst that generates the most ancient stellar populations makes the gas density quickly drop below a critical threshold, under which the star formation stops. The occurrence of such a sudden decrease in star formation was first seen in the  $[\text{Fe}/\text{O}]$  versus  $[\text{O}/\text{H}]$  data by [Gratton et al. \(1996\)](#), see also [Fuhrmann 1998, 2011](#)). The thin disc forms later, out of a second, almost independent infall episode on time scales that range from less than 3 Gyr for the inner disc to nearly a Hubble time for the outer regions (equation 2 in [Romano et al. 2000](#)). This ‘inside-out’ formation of the disc ensures the establishment of radial abundance gradients ([Larson 1976](#); [Matteucci & François 1989](#)). The adopted star formation rate is proportional to both the gas and the total surface mass density (see [Chiappini et al. 2001](#), their equation 2). The efficiency of star formation is maximum during the halo/thick-disc phase; during the thin-disc phase, it dwindles and becomes a function of the distance from the Galactic centre (see [Spitoni et al. 2015](#), and references therein). The adopted IMF is that of [Kroupa \(2002\)](#), with a slope  $\alpha = 1.7$  in the high-mass domain ( $\alpha = 1.35$  for the extrapolated [Salpeter 1955](#) law), normalized to unity in the  $0.1\text{--}100 M_{\odot}$  stellar mass range<sup>3</sup>. Hereinafter, this IMF will be referred to as the ‘canonical IMF’.

of the abundances by number on a logarithmic scale relative to the solar reference value, while  $X/Y$  refers to the ratio of the abundances by mass.

<sup>2</sup> [Henkel & Mauersberger \(1993\)](#) reached similar conclusions by relying on less refined chemical evolution models and stellar yields.

<sup>3</sup> Many authors have argued that a slope steeper than [Salpeter’s](#) has to be preferred for the local field star IMF independently from chemical evolution arguments; see, e.g., [Scalo \(1986\)](#); [Czekaj et al. \(2014\)](#); [Rybicki & Just \(2015\)](#); [Mor et al. \(2017\)](#); [Jeřábková et al. \(2018\)](#).

The two-infall model has proven able to meet the minimal set of observational constraints which should be honored by any successful Galactic chemical evolution model, namely: the surface densities of gas, stars and total matter in the solar vicinity, as well as their radial profiles; the present-day rates of star formation, infall, core-collapse and type Ia SNe in the Galaxy; the fractional contribution of metal-poor stars to the total stellar mass in the solar neighbourhood; the solar abundances; the trends of the abundances of different elements with respect to Fe as a function of  $[\text{Fe}/\text{H}]$ ; the degree of deuterium astration in the solar vicinity; the radial abundance gradients of all the major chemical species (see, e.g., Chiappini et al. 2001; Romano et al. 2006, 2010; Cescutti et al. 2007, for a discussion of the model results).

The adopted model, like all other pure chemical evolution models in the literature, makes use of simple, heuristic recipes to treat complex processes, such as gas accretion, cooling, star formation, and thermal feedback from stars. It does not include complex dynamical processes, such as radial stellar migration (but see Spitoni et al. 2015), and does not deal self-consistently with chemical inhomogeneities. However, it is extremely efficient in terms of computational costs and allows a quick exploration of the free parameter space. Therefore, since our main scope here is to test the effect of different nucleosynthesis prescriptions on the model predictions, and since we are mostly concerned with average behaviours, similarly to other authors (Nomoto et al. 2013; Prantzos et al. 2018) we regard the pure chemical evolution model as the optimal tool to comply with our requests.

## 2.2 The SMG model

We adopt the one-zone model for the typical SMG discussed in Romano et al. (2017) and Zhang et al. (2018). The model relies on the evolutionary sequence advocated by Toft et al. (2014), according to which SMGs are the precursors of passively-evolving massive elliptical galaxies. Fresh gas is accreted at early times on a short time scale at an exponentially decreasing rate,

$$\frac{d\mathcal{M}_{\text{inf}}}{dt} \propto e^{-t/\tau}, \quad (1)$$

where  $\mathcal{M}_{\text{inf}} = 4 \times 10^{11} M_{\odot}$  is the total baryonic mass accreted by the system and  $\tau = 50$  Myr is the infall time scale. The gas forms stars following a Kennicutt-Schmidt law,

$$\psi(t) = \nu \mathcal{M}_{\text{gas}}^k(t), \quad (2)$$

where  $\nu$  is the star formation efficiency,  $k = 1$  and  $\mathcal{M}_{\text{gas}}(t)$  is the mass of neutral gas available for star formation at each time (Schmidt 1959; Kennicutt 1998). The star formation is halted when a stellar mass  $\mathcal{M}_{\text{stars}} \approx 2 \times 10^{11} M_{\odot}$  is attained; a strong galactic wind triggered by SN explosions and AGN activity is supposed to clean the galaxy of its residual gas at this point. We consider a rather continuous or a bursty star formation regime, as well as a canonical or a top-heavy IMF ( $x = 1.1$  in the high-mass domain), and vary the duration of the star formation episode(s). We compare the model outputs in the different cases.

## 2.3 Nucleosynthesis prescriptions

In our computations the instantaneous recycling approximation is relaxed, i.e. we take into account in detail the finite stellar lifetimes. This is necessary in order to treat properly elements that are produced on different time scales by stars of different initial masses and various chemical compositions. The adopted nucleosynthesis

prescriptions are summarized in Table 1 and briefly discussed in the remainder of this section; a more thorough description can be found in the original papers.

### 2.3.1 Single stars

The stellar yields for low- and intermediate-mass stars (LIMS;  $1 \lesssim m/M_{\odot} \lesssim 6$ ) are either from Karakas (2010) or from Ventura et al. (2013). The latter authors also provide detailed yields for super-asymptotic giant branch (AGB) stars ( $6 \lesssim m/M_{\odot} \lesssim 8-9$ ) and (unpublished) yields for super-solar metallicity stars; both ingredients are often missing from GCE calculations. The nucleosynthetic yields for super-AGB stars computed by Doherty et al. (2014a,b) are used to complement the LIMS grid of Karakas (2010), apart from one model where this super-AGB contribution is set to zero (model MWG-02). Although the stellar mass range covered by super-AGB stars is quite modest, they are found to contribute non-negligible amounts of  $^{14}\text{N}$  on a galactic scale (see Section 3).

For massive stars, we adopt the grid of yields suggested by Nomoto et al. (2013), largely based on work published in Kobayashi et al. (2006, 2011) and extending to super-solar metallicities (models from MWG-01 to MWG-04, and model SMG-01). These yields account for some important physical processes that impact deeply the nucleosynthetic outcome of a star, such as mass loss, the ‘mixing and fallback’ process (Umeda & Nomoto 2002, and references therein), and the occurrence of highly energetic explosions (the so-called hypernovae, according to the terminology first introduced by Paczyński 1998). In particular, all stars above  $20 M_{\odot}$  are assumed to explode as hypernovae in model MWG-04, while they end up as ordinary core-collapse SNe in the other models. The important effects of stellar rotation, however, are not accounted for in the Nomoto et al.’s grid. Therefore, we also implement in our GCE code Limongi & Chieffi’s (2018) recommended yield set (set R), where: (i) mass loss and (ii) rotation are taken into account; (iii) stars with initial mass in the range  $13-25 M_{\odot}$  eject  $0.07 M_{\odot}$  of  $^{56}\text{Ni}$  after going through mixing and fallback in the inner SN regions; (iv) more massive objects fully collapse to black holes, which results in a null injection of Fe from  $m > 30 M_{\odot}$  stars<sup>4</sup>.

All the adopted yields are dependent on the initial mass and metallicity of the stars. Since they are necessarily computed for a limited number of points in the  $(m, Z)$  space, some interpolation in mass and metallicity has to be performed between published adjacent values. In particular, although we implement in the code up-to-date nucleosynthesis prescriptions for super-AGB stars, a most uncertain interpolation of the yields is still required in the mass range pertaining to low-mass core-collapse SNe ( $\sim 9-12 M_{\odot}$ ). On top of that, when adopting the Nomoto et al. (2013) yield sets for metallicities  $Z \neq 0$ , extrapolation is needed from 40 to  $100 M_{\odot}$ . Possible spurious effects can be introduced as artifacts of the interpolation/extrapolation procedures, and one should keep this in mind when comparing GCE model predictions to observations. Denser grids of stellar yields are the only way to overcome this problem.

### 2.3.2 Binary systems

The nucleosynthetic outcome of binary systems ending their lives as type Ia SNe is included in our models: we adopt the

<sup>4</sup> In models MWG-11 and MWG-12, the mass range for full collapse to black holes is reduced to  $60-100 M_{\odot}$  for  $[\text{Fe}/\text{H}] \geq -1$ .

**Table 1.** Nucleosynthesis prescriptions for different models.

| Model <sup>a</sup> |               | LIMS                                | Super-AGB stars          | Massive stars                         | $v_{\text{rot}}$<br>(km s <sup>-1</sup> ) | Hypernovae | Novae |
|--------------------|---------------|-------------------------------------|--------------------------|---------------------------------------|---|------------|-------|
| Milky Way          | Prototype SMG |                                     |                          |                                       |   |            |       |
| MWG-01             | SMG-01        | Karakas (2010)                      | Doherty et al. (2014a,b) | Nomoto et al. (2013)                  | 0   | ✗          | ✗     |
| MWG-02             | –             | Karakas (2010)                      | –                        | Nomoto et al. (2013)                  | 0   | ✗          | ✗     |
| MWG-03             | –             | Ventura et al. (2013) & unpublished |                          | Nomoto et al. (2013)                  | 0   | ✗          | ✗     |
| MWG-04             | –             | Ventura et al. (2013) & unpublished |                          | Nomoto et al. (2013)                  | 0   | ✓          | ✗     |
| MWG-05             | –             | Ventura et al. (2013) & unpublished |                          | Limongi & Chieffi (2018) <sup>b</sup> | 300                                       | ✗          | ✗     |
| MWG-06             | –             | Ventura et al. (2013) & unpublished |                          | Limongi & Chieffi (2018) <sup>b</sup> | 150                                       | ✗          | ✗     |
| MWG-07             | –             | Ventura et al. (2013) & unpublished |                          | Limongi & Chieffi (2018) <sup>b</sup> | 0   | ✗          | ✗     |
| MWG-08             | SMG-08        | Karakas (2010)                      | Doherty et al. (2014a,b) | Limongi & Chieffi (2018) <sup>b</sup> | 300                                       | ✗          | ✗     |
| MWG-09             | SMG-09        | Karakas (2010)                      | Doherty et al. (2014a,b) | Limongi & Chieffi (2018) <sup>b</sup> | 150                                       | ✗          | ✗     |
| MWG-10             | –             | Karakas (2010)                      | Doherty et al. (2014a,b) | Limongi & Chieffi (2018) <sup>b</sup> | 0   | ✗          | ✗     |
| MWG-11             | SMG-11        | Ventura et al. (2013) & unpublished |                          | Limongi & Chieffi (2018) <sup>c</sup> | var <sup>d</sup>                          | ✗          | ✓     |
| MWG-12             | SMG-12        | Karakas (2010)                      | Doherty et al. (2014a,b) | Limongi & Chieffi (2018) <sup>c</sup> | var <sup>d</sup>                          | ✗          | ✓     |

*Notes.* <sup>a</sup>We identify a particular model with the notation XXX-YY, where XXX individuates the galaxy (MWG: Milky Way galaxy, SMG: submillimeter galaxy) and YY is a number referring to the selected yield set combination. All different nucleosynthesis prescriptions have been tested against the Milky Way data, whilst only a subset of prescriptions has been used in SMG models. <sup>b</sup>We adopt their recommended yield set (set R). <sup>c</sup>Their set R is used for [Fe/H] < -1, while for [Fe/H] ≥ -1 the mass range for full collapse to black holes is reduced (60–100 M<sub>⊙</sub>). <sup>d</sup> $v_{\text{rot}} = 300 \text{ km s}^{-1}$  for [Fe/H] < -1,  $v_{\text{rot}} = 0$  for [Fe/H] ≥ -1.

single-degenerate scenario (Matteucci & Recchi 2001, and references therein) for the progenitors and nucleosynthetic yields from Iwamoto et al. (1999).

While type Ia SNe contribute negligible amounts of CNO nuclei to the interstellar medium, classical nova explosions could significantly impact the evolution of the abundances of <sup>13</sup>C, <sup>15</sup>N and <sup>17</sup>O on a Galactic scale (see José & Hernanz 2007, for a review).

The nova contribution to the synthesis of <sup>13</sup>C, <sup>15</sup>N and <sup>17</sup>O is included in two of our Milky Way models (models MWG-11 and MWG-12) by assuming average yields per nova system, similarly to what is done in Romano et al. (2017, see next paragraphs). Models SMG-11 and SMG-12, that formally share the same nucleosynthesis prescriptions with, respectively, model MWG-11 and model MWG-12, do not include a nova contribution in practice: in fact, before a newborn nova system can give rise to strong enough outbursts, it is necessary to wait at least 1 Gyr to ensure that the white dwarf has sufficiently cooled down (see below) and no SMG is expected to be forming stars on time scales longer than this. Therefore, there is basically no room for any CNO isotope pollution from novae in SMGs.

In models MWG-11, MWG-12, SMG-11 and SMG-12 nova nucleosynthesis is implemented following the prescriptions of Romano et al. (1999, 2017, and references therein), as briefly recalled hereunder; the interested reader is referred to the original papers for more details:

The rate of formation of nova systems at a given time  $t$  is computed as a fraction  $\alpha$  of the white dwarf birth rate at a previous time  $t - \Delta t$ , where  $\Delta t = 1 \text{ Gyr}$  is a suitable average time delay that guarantees that the white dwarfs cool down to temperatures low enough to ensure strong outbursts. The free parameter  $\alpha$  is assumed to be constant in time (but see Grisoni et al. 2019) and set to reproduce the current nova outburst rate in the Galaxy.

Each nova system is assumed to experience  $10^4$  powerful eruptions on an average (Bath & Shaviv 1978).

The average masses ejected in the form of <sup>13</sup>C, <sup>15</sup>N and <sup>17</sup>O in each outburst are fixed by the request that the observed declining trends of <sup>12</sup>C/<sup>13</sup>C, <sup>14</sup>N/<sup>15</sup>N and <sup>18</sup>O/<sup>17</sup>O in the last 4.5 Gyr in the solar vicinity are reproduced. For model MWG-11 (MWG-12), these masses are:  $M_{13\text{C}}^{\text{ejec}} = 4 (2) \times 10^{-7} M_{\odot}$ ,  $M_{15\text{N}}^{\text{ejec}} = 5 (6.5) \times 10^{-8} M_{\odot}$

and  $M_{17\text{O}}^{\text{ejec}} = 3 (1.5) \times 10^{-8} M_{\odot}$ . These quantities are in reasonable agreement with those emerging from hydrodynamic nova models, though a high variability is found in the theoretical nova yields in dependence of the parameters adopted to produce the outburst (see figure 6 in Romano et al. 2017, and the relevant discussion therein).

### 3 RESULTS

In the following, we first present our GCE model results in comparison with up-to-date CNO measurements in the Milky Way and select the stellar yields that guarantee the best fit to the Galactic data (Section 3.1). In the second place, we analyse a reduced set of models in comparison to CNO data for a sample of SMGs caught at the peak of their star formation activity and make some considerations about the shape of the IMF in these extreme starbursts (Section 3.2).

#### 3.1 Milky Way galaxy

##### 3.1.1 Abundance ratios of solar neighbourhood stars

Low-mass stars have lifetimes comparable to the age of the universe. Therefore, they are fossils bearing the imprints of the chemical enrichment processes that shaped their host galaxies from the very beginning.

It is well documented, though, that small mass field stars climbing the upper red giant branch undergo some important abundance changes. The original composition of their outer layers is modified markedly: the abundance of <sup>14</sup>N increases, at the expenses of that of <sup>12</sup>C, and the <sup>12</sup>C/<sup>13</sup>C ratio decreases to values close to, though higher than, the equilibrium value (e.g. Gratton et al. 2000). Unluckily, limitations imposed by current observational capabilities prevent any firm conclusion about the oxygen isotope ratios (e.g. Lebzelter et al. 2015). Unusually high C abundances in some cases may be attributable to mass transfer from a post-AGB companion across a binary system via Roche lobe overflow (Lucatello et al. 2005, and references therein). Last but not least, some low-metallicity stars currently found in the solar neighbourhood have likely been accreted from dwarf satellites and, thus, re-



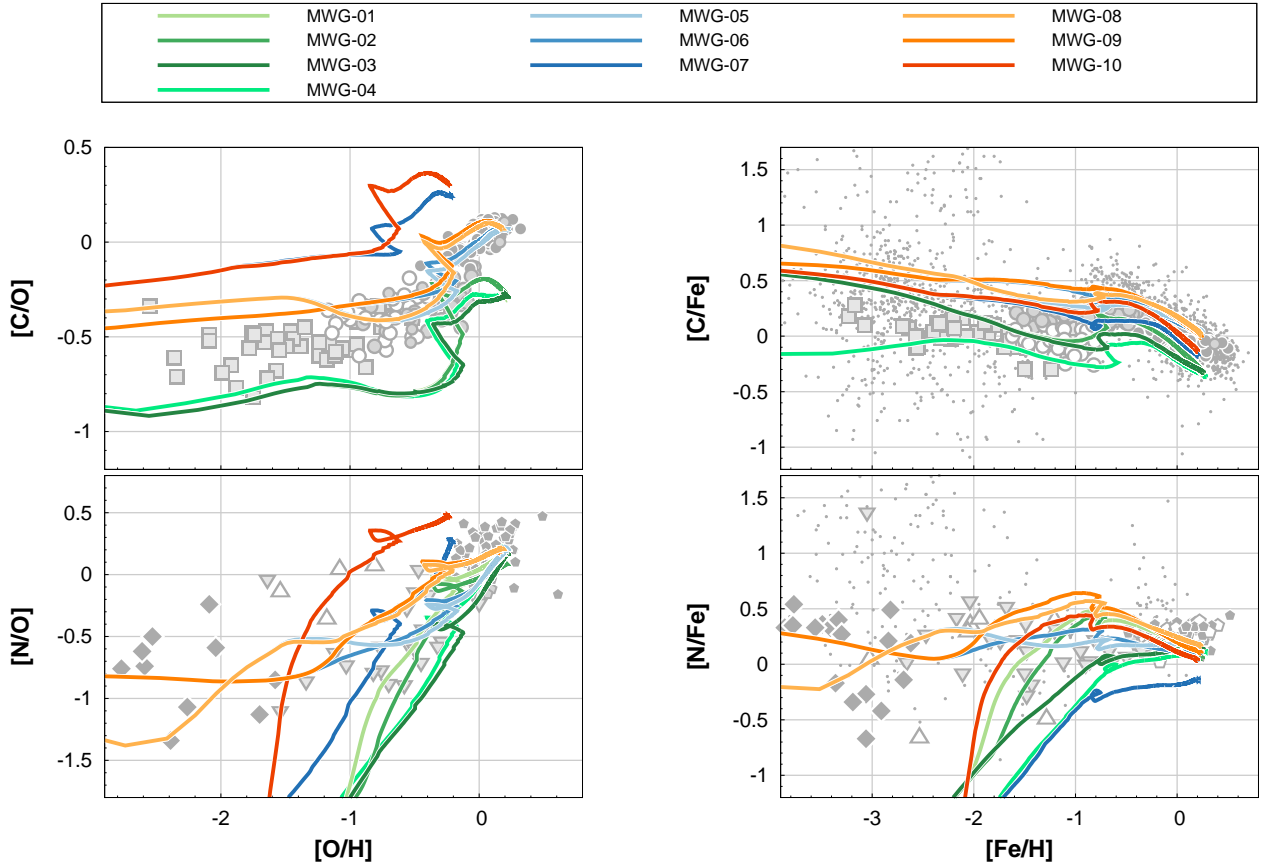


**Figure 1.** Left-hand panels:  $[C/O]$ – $[O/H]$  (top) and  $[N/O]$ – $[O/H]$  (bottom) diagrams for solar neighbourhood stars. Data for carbon are from Nissen et al. (2014, small dark-grey circles: thin-disc stars; small light-grey circles: thick-disc stars; medium-sized light-grey circles: high- $\alpha$  halo stars; medium-sized empty circles: low- $\alpha$  halo stars) and Amarsi et al. (2019, light-grey squares); data for nitrogen are from Israelian et al. (2004, upside-down triangles), Spite et al. (2005, diamonds), Roederer et al. (2014, empty triangles) and Suárez-Andrés et al. (2016, small dark-grey pentagons: thin-disc stars; small light-grey pentagons: thick-disc and halo stars; medium-sized empty pentagons: stars that could not be ascribed to a specific Galactic component). Right-hand panels:  $[C/Fe]$ – $[Fe/H]$  (top) and  $[N/Fe]$ – $[Fe/H]$  (bottom) diagrams for solar neighbourhood stars. Data as left-hand panels; also plotted are data from the SAGA database and Hypatia catalog (Suda et al. 2008; Hinkel et al. 2014, respectively, dots). See the text for a discussion of the data. In all panels, the model predictions (solid lines) are color-coded according to the adopted nucleosynthesis prescriptions (see Table 1). In this and the following figure observed and theoretical abundance ratios are normalized to solar values from Asplund et al. (2009).

flect distinct evolutionary paths. If observed stellar samples are not cleaned off for these effects, the comparison between GCE model predictions and observations via widely-used diagnostic diagrams, such as  $[C/Fe]$  versus  $[Fe/H]$  or  $[N/O]$  versus  $[O/H]$ , can easily lead to misinterpretation. It is, thus, advisable to rely on statistically significant samples of single, Sun-like stars, formed *in situ* and, possibly, analysed homogeneously.

**3.1.1.1  $[X/Fe]$  versus  $[Fe/H]$  plots.** The grey dots in Fig. 1, right-hand panels, show the  $[C/Fe]$  and  $[N/Fe]$  abundance ratios (upper and lower panel, respectively) of solar neighbourhood stars in the SAGA database (Suda et al. 2008) and Hypatia catalog (Hinkel et al. 2014). For illustration purposes, we plot stars in different evolutive stages, as well as binary stars: as expected, a large dispersion is seen in the data at all metallicities. No attempts are made to homogenize the data, that come from different sources, except for a rescaling to the same solar abundances (taken from Asplund et al. 2009 in this work).

Symbols in different shades of grey represent measurements for unevolved stars from Israelian et al. (2004, upside-down trian-

gles), Spite et al. (2005, diamonds), Nissen et al. (2014, circles), Roederer et al. (2014, triangles), Suárez-Andrés et al. (2016, pentagons) and Amarsi et al. (2019, squares).

Nissen et al. (2014) have determined precise C (and O) abundances for 151 F and G main-sequence stars with metallicities in the range  $-1.6 < [Fe/H] < 0.5$ , classified into four different populations: thin-disc, thick-disc, high- $\alpha$  halo and low- $\alpha$  halo stars (shown, respectively, as small dark-grey, small light-grey, medium-sized light-grey and empty circles in Fig. 1, upper panels). These authors have used plane parallel (1D) model atmospheres for their analysis and applied non-LTE corrections to the abundances derived from the CI  $\lambda\lambda 5052, 5380$  lines and  $\lambda 7774$  OI triplet. As seen from Fig. 1, upper right-hand panel, these precise abundances define a tight trend in the  $[C/Fe]$ – $[Fe/H]$  plane. Under the reasonable assumption (Nissen et al. 2014, and references therein) that the low- $\alpha$  halo stars formed in dwarf galaxies that were later accreted by the Milky Way and, thus, do not trace the local enrichment history, the observed trend for  $[Fe/H] > -1.5$  is fitted at best by models MWG-07 and MWG-10, that assume the yields by Limongi & Chieffi (2018) for non-rotating massive stars

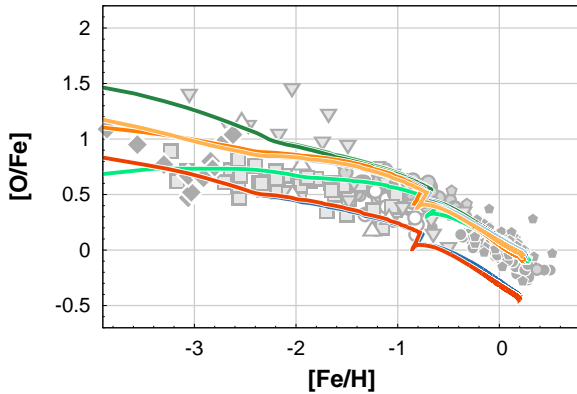


**Figure 2.**  $[O/Fe]$ – $[Fe/H]$  diagram for solar neighbourhood stars. Data are from [Israelian et al. \(2004, upside-down triangles\)](#), [Spite et al. \(2005, diamonds\)](#), [Nissen et al. \(2014, small dark-grey circles: thin-disc stars; small light-grey circles: thick-disc stars; medium-sized light-grey circles: high- \$\alpha\$  halo stars; medium-sized empty circles: low- \$\alpha\$  halo stars\)](#), [Roederer et al. \(2014, empty triangles\)](#), [Bertran de Lis et al. \(2015, small dark-grey pentagons: thin-disc stars; small light-grey pentagons: thick-disc and halo stars; medium-sized empty pentagons: stars that could not be ascribed to a specific Galactic component\)](#) and [Amarsi et al. \(2019, light-grey squares\)](#). The model predictions (*solid lines*) are color-coded according to the adopted nucleosynthesis prescriptions (see Table 1 and explanatory legend in Fig. 1).

(see Table 1). Marginal agreement is obtained by the models that adopt the yields by [Limongi & Chieffi \(2018\)](#) for rotating massive stars (models MWG-05, MWG-06, MWG-08, MWG-09) and by models MWG-01 and MWG-02, that assume the yields by [Nomoto et al. \(2013\)](#) for (non-rotating) massive stars without hypernovae, as well as the yields by [Karakas \(2010\)](#) for LIMS (C production from super-AGB stars as issued in [Doherty et al. 2014a,b](#) turns out to be negligible).

The behaviour of C (and O) abundances at lower metallicities has been reassessed recently by [Amarsi et al. \(2019\)](#). Basing on 3D, non-LTE results for 39 turn-off stars with  $[Fe/H] \leq -1.5$ , they find that  $[C/Fe]$  is almost solar and stays nearly flat with metallicity. Interestingly, the abundances of three stars previously identified as carbon-enhanced stars with  $[C/Fe]$  in excess of 1 are significantly revised downwards, to  $[C/Fe] \approx 0.1$ – $0.3$  (see [Amarsi et al. 2019](#), their section 4, for a thorough discussion). When compared with our model predictions, these new measurements seem to point to the need for some hypernova pollution at low metallicities (cfr. the predictions from model MWG-04, in which all stars above  $20 M_{\odot}$  end up with a hypernova explosion, with those from model MWG-03, which is the same as model MWG-04, but with all massive stars exploding as ordinary SNe; Fig. 1, upper right-hand panel).

We now examine the behaviour of  $[N/Fe]$  versus  $[Fe/H]$ . An inspection of Fig. 1, lower right-hand panel, immediately shows that a significant dispersion characterizes the data at low metallicities, even when only unevolved stars are considered ([Israelian et al. 2004](#); [Spite et al. 2005](#); [Roederer et al. 2014](#)). Below  $[Fe/H] \sim -1.5$ , some observations can be explained only by invoking a significant primary N production from massive stars (a well-known result; see previous work by [Matteucci 1986](#); [Chiappini et al. 2006](#); [Romano et al. 2010](#); [Prantzos et al. 2018](#)). However, a few low  $[N/Fe]$  values point to a milder N enrichment. The N yields of massive stars depend critically on the stellar rotational velocity, therefore, a large dispersion in the N abundances would naturally arise during the Galactic halo assembly, because

of the highly inhomogeneous evolution: regions polluted by non-rotating massive stars will display a N content significantly lower than regions where matter was processed through one or more fast rotators. Assessing the evolution of the CNO elements in a more realistic, inhomogeneous medium would be extremely valuable, and can be done by means of detailed hydrodynamical simulations. A quantitative explanation of the observed scatter, however, is beyond the scope of the present work and will be addressed in a future paper. It suffices to note here that the dispersion is sensibly reduced at disc metallicities, where reliable N abundances can be derived for statistically significant samples of dwarf stars from the  $\lambda 3360$  NH molecular band ([Suárez-Andrés et al. 2016](#)). Overall, we find that models MWG-05 and MWG-06, with yields from [Limongi & Chieffi \(2018\)](#) for rotating massive stars and from [Ventura et al. \(2013\)](#) for LIMS and super-AGB stars, provide an excellent fit to the average  $[N/Fe]$  ratios over the full range of metallicities.

The run of  $[O/Fe]$  as a function of  $[Fe/H]$  is shown in Fig. 2. All models provide an adequate fit to the observed trend, apart from models MWG-07 and MWG-10, that are computed with the yields from non-rotating massive stars by [Limongi & Chieffi \(2018, their set R\)](#), which severely underestimate the  $[O/Fe]$  ratios of disc stars. If the 3D oxygen abundances by [Amarsi et al. \(2019\)](#) have to be given a higher weight, it is possible that in the early Galaxy a large fraction of high-mass stars exploded as hypernovae, with an energy release substantially higher than that of standard SNe (cfr. the predictions from model MWG-04, in which all stars above  $20 M_{\odot}$  end up as hypernovae, with those from model MWG-03, in which the same stars explode as normal core-collapse SNe).

**3.1.1.2  $[X/O]$  versus  $[O/H]$  plots.** The  $[C/O]$ – $[O/H]$  and  $[N/O]$ – $[O/H]$  diagrams shown in Fig. 1, left-hand panels, are particularly useful. At low metallicities, they trace the enrichment from massive stars with minimum linkage to one of the most uncertain parameters of stellar evolution, namely, the location of the mass cut (in most extant one- and two-dimensional models of the latest stages of massive star evolution, this is the boundary between the collapsed core and the ejected mantle); by contrast, the choice of the mass cut influences considerably the theoretical trends in the  $[X/Fe]$  versus  $[Fe/H]$  planes. At disc metallicities, the rise in  $[C/O]$  and  $[N/O]$  can be related to the late contribution to C and N production from low-metallicity, low-mass stars, and directly compared to the release of C and N from relatively more metal-rich massive stars, which occurs on much shorter time scales.

Moreover, from a theoretical point of view, the trends with metallicity as gauged by oxygen abundance are free from the uncertainties that arise from the inclusion of type Ia SNe in the models (these systems produce a large fraction of the solar iron, but negligible amounts of oxygen). However, from a spectroscopist’s standpoint, the abundance estimates are less robust for O than for Fe. Oxygen abundances are affected by non-negligible non-LTE corrections when derived from the O I triplet, and by 3D effects (as well as a Ni I blend) when derived from the forbidden [O I] line at  $6300 \text{ \AA}$ ; the latter line is also too weak to be detectable in the majority of halo stars (see [Nissen et al. 2014](#), and references therein). Furthermore, the O abundances of metal-poor stars derived from near-UV OH lines (such as those used by [Israelian et al. 2004](#)) are found to be systematically higher than the ones obtained from other indicators (see Fig. 2).

With all the above-mentioned possible shortcomings in mind, we compare the trends predicted by our GCE model under different nucleosynthesis prescriptions (colored lines in Fig. 1) to the

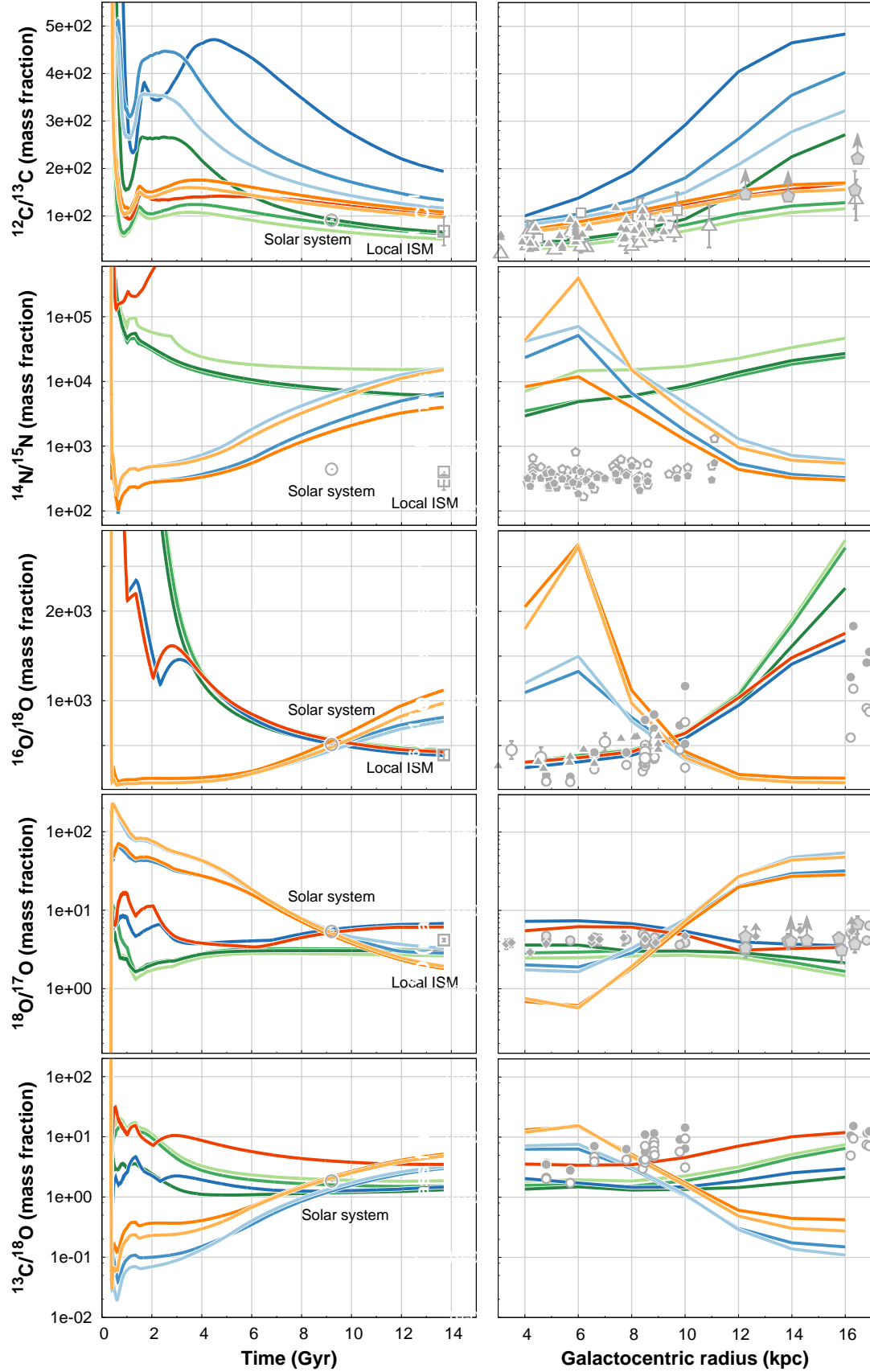


**Figure 3.** *Left-hand panels:* evolution of different CNO isotope ratios in the solar vicinity. *Right-hand panels:* corresponding present-time gradients across the Milky Way disc. Theoretical predictions (solid lines) are color-coded according to the adopted nucleosynthesis prescriptions (see Table 1 and explanatory legend in Fig. 1). Data (grey symbols) sources are given in the text.



observational data from [Israelian et al. \(2004\)](#), [Spite et al. \(2005\)](#), [Nissen et al. \(2014\)](#), [Roederer et al. \(2014\)](#), [Suárez-Andrés et al. \(2016\)<sup>5</sup>](#) and [Amarsi et al. \(2019\)](#) discussed in the previous paragraphs. Overall, the most appropriate yields appear to be those of [Limongi & Chieffi \(2018\)](#) for rotating massive stars coupled to those of [Ventura et al. \(2013\)](#) for LIMS and super-AGB stars, i.e. models MWG-05 and MWG-06. In particular, the relatively low N yields by [Ventura et al. \(2013\)](#) guarantee a better fit to the observed  $[N/O]$  ratios for  $[O/H] > -1.2$ , that is when the contributions from super-AGB stars first, and LIMS right after, start to become relevant.

### 3.1.2 CNO isotope ratios in space and time in the Galaxy

The determination of isotopic abundances in stars is limited to a handful of chemical species. For CNO elements, it can be made mostly in brilliant, giant stars. These, however, can have the original composition of their atmospheres altered by internal processes. It is thus convenient to resort to measurements of gas-phase isotopic abundances in interstellar clouds, though they provide only snapshots in time and, hence, no information about the past evolution that led to the observed configuration.

Radio observations are the prime tools for exploring the present-day gradients of  $^{12}C/^{13}C$ ,  $^{14}N/^{15}N$ ,  $^{16}O/^{18}O$ ,  $^{18}O/^{17}O$  and  $^{13}C/^{18}O$  in the disc of our Galaxy. For the purpose of comparison with the predictions of our GCE model, we take the data from: (i) the compilation of [Wilson & Rood \(1994\)](#), based on results from molecular transitions of carbon monoxide and formaldehyde (small filled triangles in Fig. 3, upper and middle right-hand panels); (ii) [Milam et al. \(2005\)](#), based on  $N = 1-0$  transitions of the CN radical (large empty triangles in Fig. 3, upper right-hand panel); (iii) [Polehampton et al. \(2005\)](#), which analysed the ground state rotational lines of the OH isotopologues (large empty circles in Fig. 3, middle right-hand panel); (iv) [Wouterloot et al. \(2008\)](#), providing a) the  $^{13}CO/C^{18}O$  gradient, from simultaneously observed  $^{13}CO$  and  $C^{18}O$   $J = 1-0$  and  $J = 2-1$  transitions (respectively, small filled and small empty circles in Fig. 3, middle and lower right-hand panels; the original data have been combined with the  $^{12}C/^{13}C$  gradient by [Milam et al. 2005](#) to trace the  $^{16}O/^{18}O$  gradient) and b) the  $^{18}O/^{17}O$  gradient, from  $J = 1-0$ ,  $2-1$  and  $3-2$  transitions of  $C^{18}O$  and  $C^{17}O$  (small light-grey circles in Fig. 3); (v) [Li et al. \(2016\)](#), which derived  $C^{18}O/C^{17}O$  abundance ratios for 13 sources spanning the Galactocentric distance range 3–16 kpc (small filled diamonds in Fig. 3); and (vi) [Colzi et al. \(2018\)](#), which targeted the  $J = 1-0$  rotational transitions of hydrogen isocyanide and hydrogen cyanide and derived the  $^{14}N/^{15}N$  ratios for both molecules (Fig. 3, the small filled and small empty pentagons are for HNC and HCN, respectively). To these we add some solid-state  $^{12}C/^{13}C$  data by [Boogert et al. \(2000\)](#), from interstellar  $CO_2$  ices – small empty squares in Fig. 3, upper right-hand panel) and preliminary  $^{12}C/^{13}C$  and  $^{18}O/^{17}O$  measurements and lower limits for outer disc targets from [Zhang et al. \(2019\)](#), in preparation, large grey pentagons in Fig. 3).

While the shapes of the present-day gradients of CNO isotope ratios in our Galaxy are reasonably well-known (with the exception of the outer disc, where only a few measurements are available; but see [Zhang et al. 2019](#), in preparation), the knowledge of the evolution of these ratios in the solar neighbourhood is tightly limited. For

the comparison with our model predictions, we rely on solar ratios from [Ayres et al. \(2013\)](#),  $^{12}C/^{13}C = 91.4 \pm 1.3$ ,  $^{16}O/^{18}O = 511 \pm 10$ ,  $^{18}O/^{17}O = 5.36 \pm 0.34$  and [Marty et al. \(2011\)](#),  $^{14}N/^{15}N = 441 \pm 6$ . These are shown as Sun symbols in Fig. 3, left-hand panels. It should be noted, however, that the Sun might have migrated to its actual position from an inner birthplace ([Wielen et al. 1996](#)) and, thus, its chemical composition might not reflect that of the local medium 4.5 Gyr ago. For the local interstellar medium, we adopt average values (large open squares in Fig. 3, left-hand panels) from the studies discussed above, namely:  $\langle^{12}C/^{13}C\rangle_{LISM} = 68 \pm 15$  ([Milam et al. 2005](#)),  $\langle^{16}O/^{18}O\rangle_{LISM} = 395 \pm 56$  ([Polehampton et al. 2005](#)),  $\langle^{18}O/^{17}O\rangle_{LISM} = 4.16 \pm 0.09$  ([Wouterloot et al. 2008](#)). For  $\langle^{14}N/^{15}N\rangle_{LISM}$ , both the low value from [Adande & Ziurys \(2012\)](#),  $290 \pm 40$  and the high value from [Colzi et al. \(2018\)](#),  $\sim 400$  are displayed.

The predictions from models MWG-01, MWG-02 and MWG-03 are in good agreement with the available  $^{12}C/^{13}C$  data both for the solar vicinity and across the disc. Should a substantial contribution to  $^{13}C$  production come from nova systems (see next section), models MWG-05, MWG-06, MWG-07, MWG-08, MWG-09 and MWG-10 could be made consistent with the observations, but the fit would worsen for models from MWG-01 to MWG-03.

Actually, in order to explain the observed decrease of the  $^{14}N/^{15}N$  ratio in the local disc over the last 4.5 Gyr, as well as its positive gradient across the disc, it is necessary that a large amount of  $^{15}N$  is supplied by some up to now neglected stellar factory. Thermonuclear runaways occurring in nova outbursts stand out as possible candidates (but see [Chin et al. 1999](#); [Pignatari et al. 2015](#)).

As regards the O isotope ratios, models in which the yields from fast-rotating massive stars are implemented during the full Galactic evolution – namely, models MWG-05, MWG-06, MWG-08 and MWG-09 – produce gradients at variance with the observations. Indeed, some theoretical arguments (see [Meynet & Maeder 1997](#)) suggest that low-metallicity stars rotate faster than high-metallicity stars, on an average. For this reason, [Prantzos et al. \(2018\)](#) introduced an initial distribution of stellar rotational velocities (IDROV) in their GCE model, in analogy with the adoption of a stellar IMF. Because of the extremely loose constraints that can be imposed on the actual IDROV, however, their choice is far from unique. In the following section, we discuss the results of our GCE model when a simple step function is adopted for the IDROV: we assume the yields corresponding to stellar models computed with  $v_{rot} = 300 \text{ km s}^{-1}$  for  $[Fe/H] < -1$  and the yields of non-rotating models at higher metallicities. In the latter case, we also set to 60–100  $M_{\odot}$ , rather than 35–100  $M_{\odot}$ , the mass range for full collapse to black holes, which guarantees a better fit to the observed O abundances of local disc stars in the framework of our model.

### 3.1.3 A possible, comprehensive evolutive scenario

From Figs. 1 and 2 discussed above, one sees that the adoption of massive star yields computed with either  $v_{rot} = 300 \text{ km s}^{-1}$  or  $v_{rot} = 150 \text{ km s}^{-1}$  results in comparable  $[C/Fe]$ ,  $[C/O]$  and  $[O/Fe]$  ratios, that differ by 0.15 dex at most, during the entire solar neighbourhood evolution. Larger differences (up to 0.5 dex at the lowest metallicities) are found between the theoretical  $[N/Fe]$  and  $[N/O]$  ratios predicted for halo stars in the two cases, while the differences cancel out at disc metallicities.

The largest contrasts arise anyway between the evolutive tracks obtained in the rotating case (whatever the value of  $v_{rot}$ ) and the non-rotating one. While nothing can be said from direct observations about the distribution of the rotational velocities of

<sup>5</sup> The O abundances for the stars in the sample of [Suárez-Andrés et al. \(2016\)](#) are taken from [Bertran de Lis et al. \(2015\)](#).

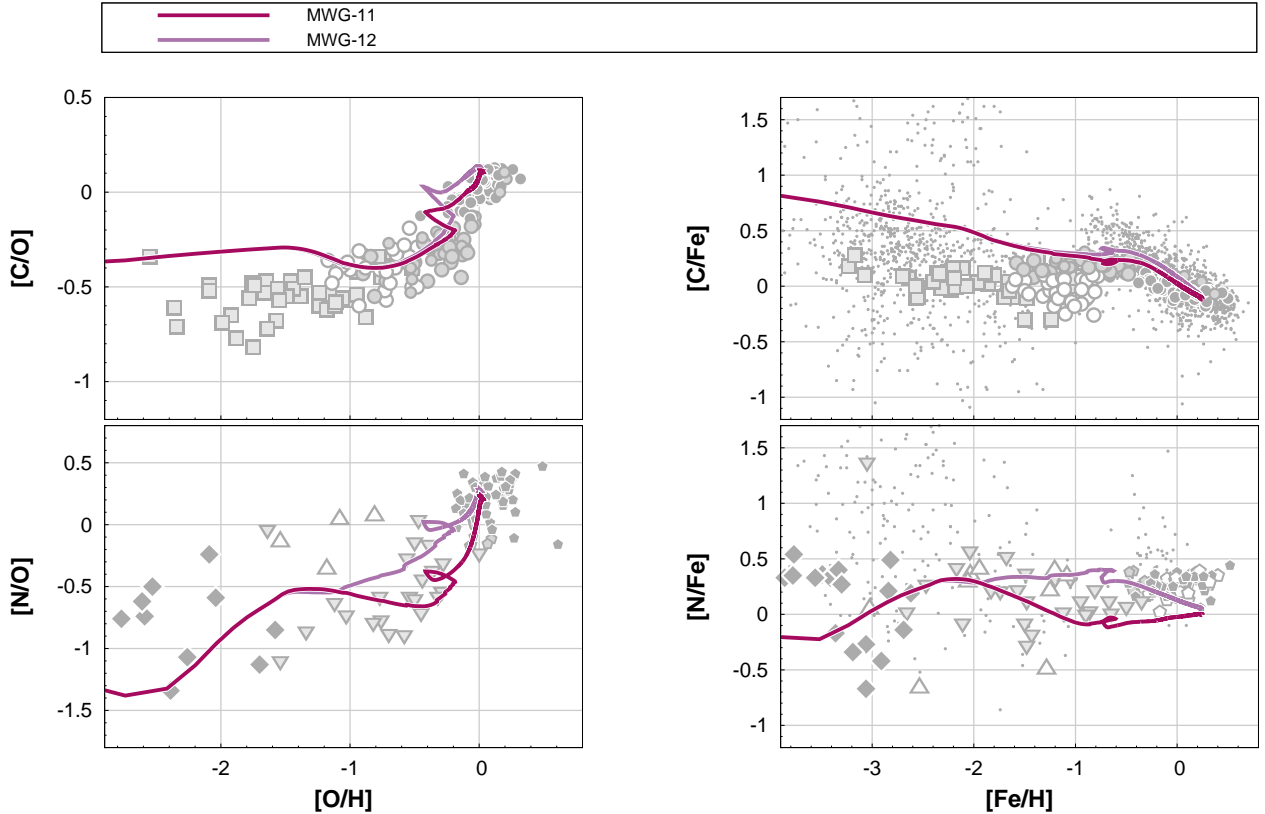


**Figure 4.** Same as Fig. 1, but the model predictions are from models MWG-11 and MWG-12 (bordeaux and lilac lines, respectively).

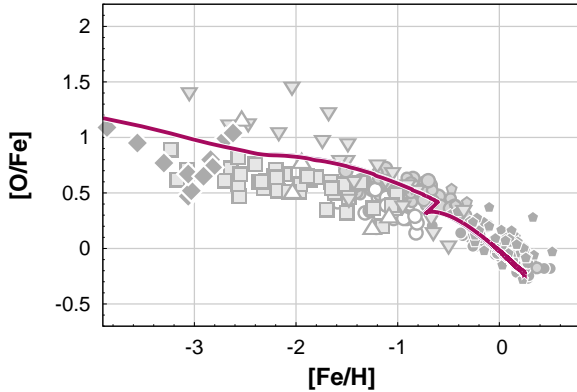


**Figure 5.** Same as Fig. 2, but shown are predictions from models MWG-11 and MWG-12 (the latter, concealed behind model MWG-11 predictions).

low-metallicity, high-mass stars, there is strong, indirect evidence from the chemical composition of unevolved halo stars that below  $[\text{Fe}/\text{H}] = -2$  most SNII progenitors must have been fast rotators: indeed, fast rotation leads to the synthesis of large amounts of primary  $^{14}\text{N}$  at low metallicities, which explains the relevant observations (see also Chiappini et al. 2006; Prantzos et al. 2018, and references therein).

Let us now throw the minor CNO isotopes into the mix (Fig. 3): the situation gets more complicated! In fact, novae – not included in models from MWG-01 to MWG-10 – may inject sig-

nificant amounts of  $^{13}\text{C}$ ,  $^{15}\text{N}$  and  $^{17}\text{O}$  in the Galactic medium on long time scales (see Romano & Matteucci 2003, and references therein). If implemented in models including fast rotators, this contribution may, in principle, reverse the trend at odds with the observations predicted for  $^{14}\text{N}/^{15}\text{N}$  and improve the agreement between predicted and observed  $^{12}\text{C}/^{13}\text{C}$  ratios. Yet, the  $^{16}\text{O}/^{18}\text{O}$  ratio is immune to changes caused by an implementation of this nucleosynthetic channel (neither  $^{16}\text{O}$  nor  $^{18}\text{O}$  are produced in appreciable amounts in nova outbursts).

From Fig. 3, middle panels, it can be seen that GCE models without fast rotators produce  $^{16}\text{O}/^{18}\text{O}$  ratios in remarkable agreement with local and inner disc data. From the more uncertain abundance determinations in the outer disc, however, it can not be excluded that a fraction of massive stars are rotating fast at large Galactocentric distances. Our GCE model predicts the current metallicity in the inner (outer) Milky Way disc to be  $Z \approx 0.016$ – $0.028$  ( $0.005$ – $0.009$ ) at  $R_G = 4$  (16) kpc (the exact value depending on the choice of the stellar yields). Thus, the overall picture is one in which the formation of fast-rotating massive stars is inhibited in environments with solar or super-solar metallicity, while it can not be excluded that a fraction of massive stars are rotating fast in regions with metallicities close to those typical of the Magellanic Clouds. Likewise from N observations, and as expected from theory (Meynet & Maeder 1997), from the  $^{16}\text{O}/^{18}\text{O}$  ratios we get an indication that fast-rotating massive stars are more common in less evolved environments. It goes without saying that more precise measurements of the  $^{16}\text{O}/^{18}\text{O}$  ratios in more populous samples of low-metallicity molecular clouds are crucial to better understand the transition from the fast-rotation to the null(or slow)-rotation

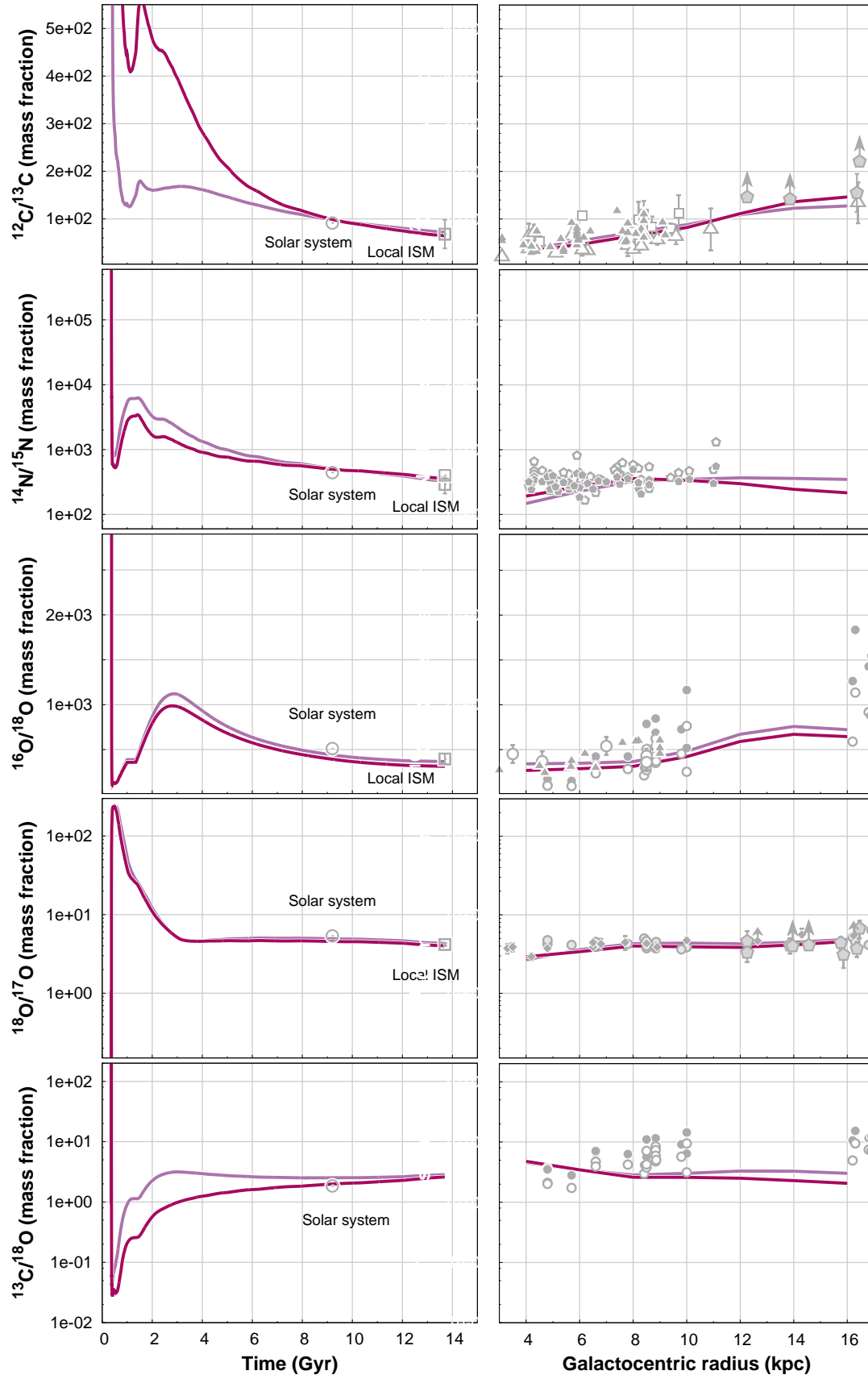


**Figure 6.** Same as Fig. 3, but shown are predictions from models MWG-11 and MWG-12 (bordeaux and lilac lines, respectively).

regime. It is worth recalling at this point that the  $^{16}\text{O}/^{18}\text{O}$  gradient in the Milky Way is determined from  $^{13}\text{CO}$  and  $\text{C}^{18}\text{O}$  transitions (Wouterloot et al. 2008) via the adoption of a  $^{12}\text{C}/^{13}\text{C}$  gradient that is poorly defined in the outer disc (see Fig. 1, upper right-hand panel). Thus, better  $^{16}\text{O}/^{18}\text{O}$  determinations call for better estimates of the  $^{12}\text{C}/^{13}\text{C}$  ratio. We will address this issue in detail in a forthcoming paper (Zhang et al. 2019, in preparation). Grids of yields computed for rotational velocities in between those considered here are also in demand.

In the remainder of this section we use what is at hand and discuss the results of two GCE models that: (i) assume a simple step function for the IDROV of core-collapse SN progenitors and (ii) take into account the production of rare isotopes during nova outbursts.

As regards the massive stars, for  $[\text{Fe}/\text{H}] = -3$  and  $[\text{Fe}/\text{H}] = -2$  we adopt the recommended yields by Limongi & Chieffi (2018, their set R) computed with  $v_{\text{rot}} = 300 \text{ km s}^{-1}$ . For  $[\text{Fe}/\text{H}] = -1$  and  $[\text{Fe}/\text{H}] = 0$ , we use the yields for non-rotating stars and reduce the mass range for full collapse to black holes from 30–100  $M_{\odot}$  to 60–100  $M_{\odot}$ , which improves the predictions about the behaviour of  $[\text{O}/\text{Fe}]$  versus  $[\text{Fe}/\text{H}]$  – and, hence, the run of  $[\text{C}/\text{O}]$  and  $[\text{N}/\text{O}]$  as a function of  $[\text{O}/\text{H}]$  – at disc metallicities in our models. The yields for LIMS and super-AGB stars are taken from Ventura et al. (2013, model MWG-11) or from Karakas (2010) and Doherty et al. (2014a,b, model MWG-12). Linear interpolation in mass and metallicity is performed between adjacent values of the yields. In both model MWG-11 and model MWG-12, nova nucleosynthesis is implemented following the prescriptions of Romano et al. (1999, 2017, and references therein; see Section 2.3.2).

The results of models MWG-11 and MWG-12 are illustrated in Figs. 4–6. From Figs. 4 and 5, it can be seen that for the main CNO isotopes the agreement with the observations is from satisfactory to very good during most of the solar neighbourhood evolution. The predicted overabundances of carbon and (to a lower extent) oxygen in the early Galaxy have to be expected and could be rectified by the inclusion of a fraction of hypernovae at low metallicities (see the discussion in Section 3.1.1). Such an energy effect would also have the advantage of redressing the well-known discrepancies between predicted and observed cobalt and zinc abundances in low-metallicity Galactic halo stars (Kobayashi et al. 2006; Romano et al. 2010; Prantzos et al. 2018).

Stars with initial masses  $m \leq 9 M_{\odot}$  do not produce  $^{16}\text{O}$  (rather, they partly destroy it in their interiors), but synthesise about one third of the solar  $^{12}\text{C}$  (30 per cent for model MWG-11, and more than 35 per cent for model MWG-12), as well as most of the solar  $^{14}\text{N}$  (65 per cent in the case of model MWG-11, and more than 70 per cent for model MWG-12). As already stressed by Carigi et al. (2005), the fractional contribution from LIMS (and super-AGB stars) and massive stars is strongly dependent on time, on the galactic region under scrutiny and, of course, on the adopted GCE model and stellar yields. Therefore, one should beware of any daring extrapolations of the rates reported above to other galaxies. In the next section, we further stress this point by discussing the results for a prototype SMG observed at high redshift.

The enrichment of  $^{13}\text{C}$  coarsely tracks that of  $^{14}\text{N}$ , with more than 50 and 70 per cent of the solar  $^{13}\text{C}$  being produced by LIMS and super-AGB stars in models MWG-11 and MWG-12, respectively. In particular, according to Karakas (2010) and Doherty et al. (2014a,b), low-metallicity intermediate- to high-mass AGB stars are effective  $^{13}\text{C}$  producers (see Fig. 7), which makes the predicted carbon isotope ratio to reach down to  $^{12}\text{C}/^{13}\text{C} \approx 130$  at the end of

the halo/thick-disc formation in model MWG-12 (Fig. 6, upper left-hand panel). Model MWG-11, that assumes the much lower  $^{13}\text{C}$  yields by Ventura et al. (2013) for the same stars, barely reaches down to  $^{12}\text{C}/^{13}\text{C} \sim 400$ , making it harder to conciliate its predictions to observations of post first dredge-up halo stars (Spite et al. 2006). At solar metallicities, the  $^{13}\text{C}$  yields from both sets of stellar models align with each other and the stars with  $m > 4 M_{\odot}$  efficiently destroy  $^{12}\text{C}$  in their interiors (see Fig. 8), which leads to converging GCE results (the slightly more pronounced decline characterising the late evolution of the carbon isotope ratio in model MWG-11 compared to model MWG-12 is due to the slightly larger  $^{13}\text{C}$  nova yield necessary to bring the predicted solar abundance of  $^{13}\text{C}$  in agreement with the observed one in model MWG-11).

The minor isotope of nitrogen,  $^{15}\text{N}$ , is destroyed in non-rotating stellar models, but it is efficiently synthesised in the presence of rotation, owing to the diffusion of matter between the H- and He-burning zones (Limongi & Chieffi 2018; Prantzos et al. 2018). However, this production is not sufficient, alone, to explain the Galactic  $^{14}\text{N}/^{15}\text{N}$  data. In this work, we fit well measurements of nitrogen isotope ratios in Milky Way targets by resorting to nova pollution (see Fig. 6), but we ought to mention that unusually high  $^{15}\text{N}$  abundances are found in some Galactic AGB stars (Hedrosa et al. 2013) and planetary nebulae (Schmidt et al. 2018). These are currently unexplained by stellar evolution theory and might call for some substantial revision of stellar physics.

The  $^{17}\text{O}$  yields are overall positive, apart from those from  $m > 20\text{--}25 M_{\odot}$  star models, that turn negative<sup>6</sup> for  $[\text{Fe}/\text{H}] \geq -1$ . As a consequence, the predicted  $^{18}\text{O}/^{17}\text{O}$  ratio decreases with time in the local disc, except in the last 4.5 Gyr, when it would mildly increase without the addition of a nova contribution. Our GCE models, including such contribution, account very well for the local evolution of this isotope ratio, as well as its Galactic gradient (see Fig. 6, second left- and right-hand panels down, respectively).

As regards  $^{18}\text{O}$ , its yields are largely positive for stars in the mass interval 13–25  $M_{\odot}$ , while out of this range the stars either destroy  $^{18}\text{O}$ , or provide smaller amounts of it. From Fig. 6, middle panels, it is seen that the evolution of the  $^{16}\text{O}/^{18}\text{O}$  isotope ratio in the Milky Way is reproduced fairly well by both models MWG-11 and MWG-12. However, in order to assess the validity of the models at relatively low metallicities, it is mandatory to obtain firmer measurements of this ratio in the external disc (see arguments set out in previous paragraphs).

### 3.2 Prototype SMG

In this section, we discuss the results of our one-zone models for the typical SMG, namely models SMG-01, SMG-08, SMG-09, SMG-11 and SMG-12 (the numbers refer to the adopted nucleosynthesis prescriptions, see Table 1). Each model is run four times, by assuming a set of three distinct star formation histories (SFHs) and two different IMFs. Specifically, we adopt: (i) a continuous star formation, mildly decreasing in time and lasting 1 Gyr, with a star formation rate of hundreds of solar masses per year, and a canonical IMF; (ii) an extremely vigorous ( $\text{SFR}_{\text{peak}} \sim 15\,000 M_{\odot} \text{ yr}^{-1}$ ), short ( $\Delta t_{\text{burst}} = 20 \text{ Myr}$ ) starburst, forming stars according to a canonical IMF; (iii) a gasping SFH, which consists of several short star formation bursts ( $\Delta t_{\text{burst}} = 50 \text{ Myr}$  each) interspersed with similarly long quiescent periods, with either a canonical or (iv) a top-

<sup>6</sup> This is true only for the yield sets by Limongi & Chieffi (2018); Nomoto et al. (2013) always report positive  $^{17}\text{O}$  yields for massive stars.

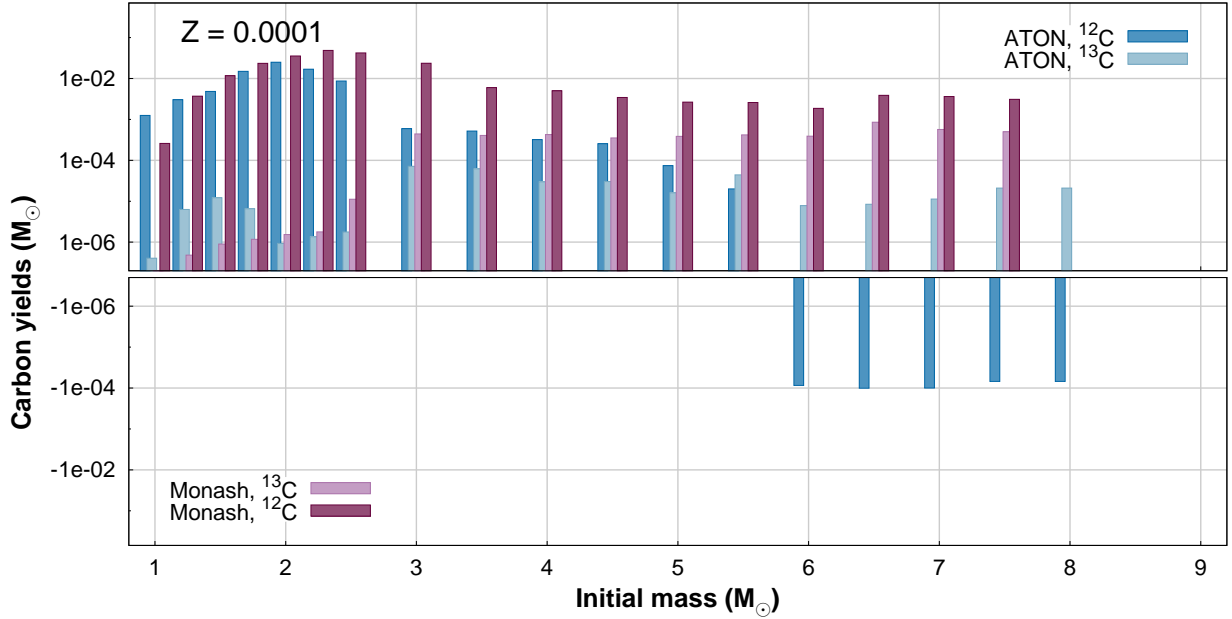


**Figure 7.** Net yields of  $^{12}\text{C}$  and  $^{13}\text{C}$  from LIMS and super-AGB stars after Ventura et al. (2013), in shades of blue, and Karakas (2010) and Doherty et al. (2014a,b), in shades of purple, for  $Z = 0.0001$ . A negative yield means the element is destroyed, rather than produced, in the star.

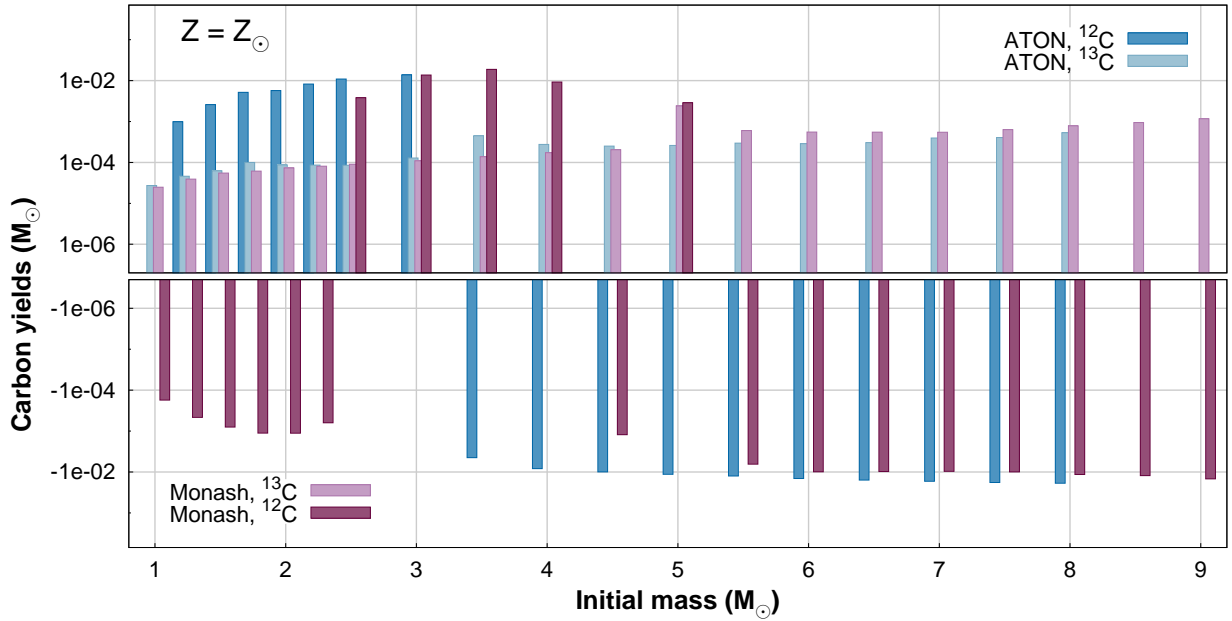


**Figure 8.** Same as Fig. 7, but for solar metallicity.

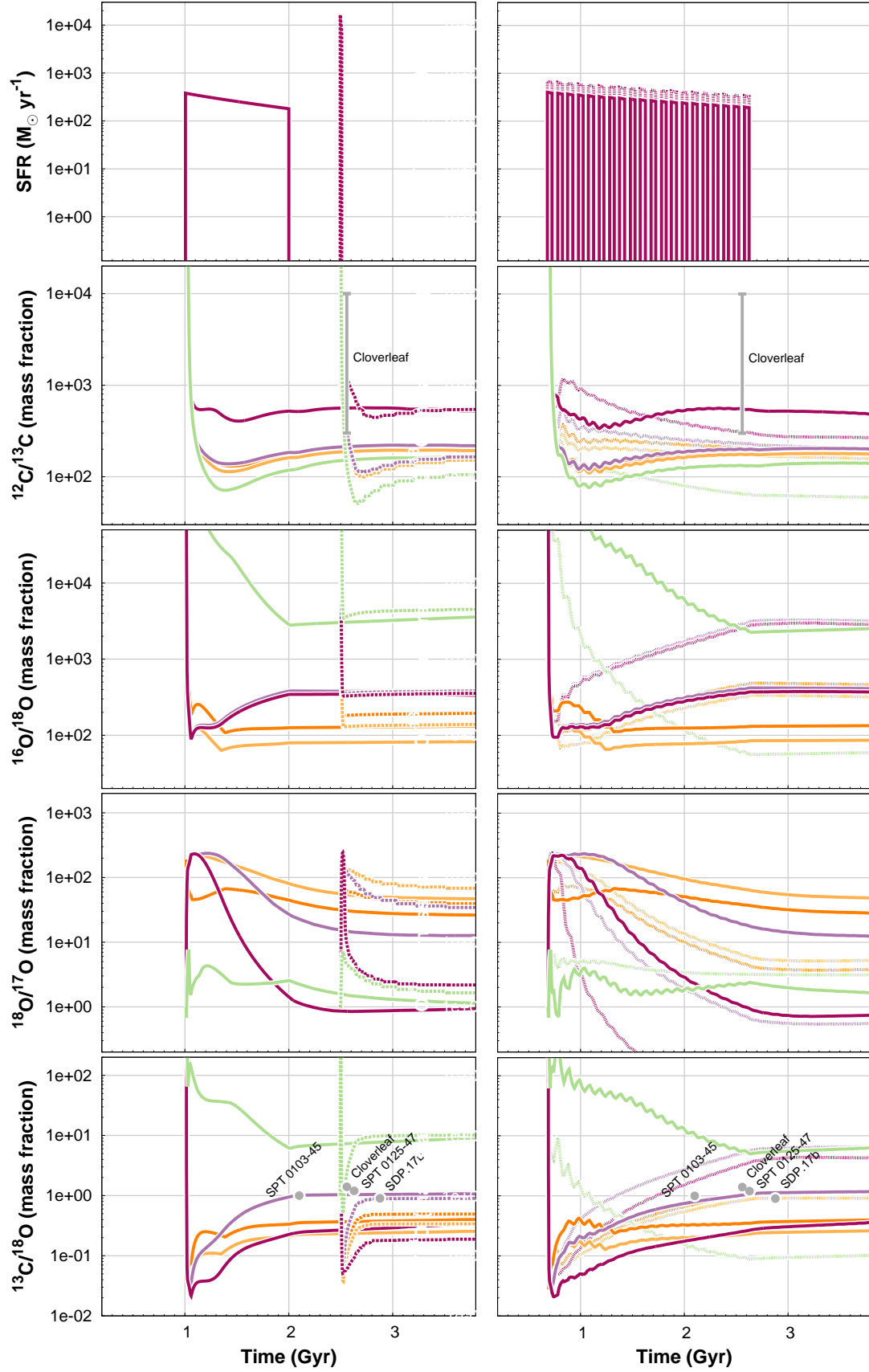
heavy IMF (see Table 2). In all cases, when the star formation stops,  $\mathcal{M}_{\text{stars}} \approx 2 \times 10^{11} M_{\odot}$  are in place.

The resulting theoretical tracks are displayed in Figs. 9 and 10, where the solid and short-dashed lines in the left-hand panels refer to case (i) and (ii), respectively, and the solid and dotted lines in the right-hand panels refer to case (iii) and (iv), respectively. The model results are further color-coded according to the adopted nucleosynthesis prescriptions: green is for model SMG-01, yellow for model SMG-08, orange for model SMG-09, purple

for model SMG-11 and lilac for model SMG-12. The values of the ratios at the time of the halt of the star formation are reported in Table 2.

The results of model SMG-01 are essentially the same as the ones discussed in Zhang et al. (2018). In that paper, because of the adoption of stellar yields that did not include the effects of rotation,  $^{13}\text{C}/^{18}\text{O}$  ratios of about unity in SMGs could only be explained by assuming an IMF skewed towards massive stars. Indeed, from Fig. 9, lower panels, and Table 2, last column, it is seen that



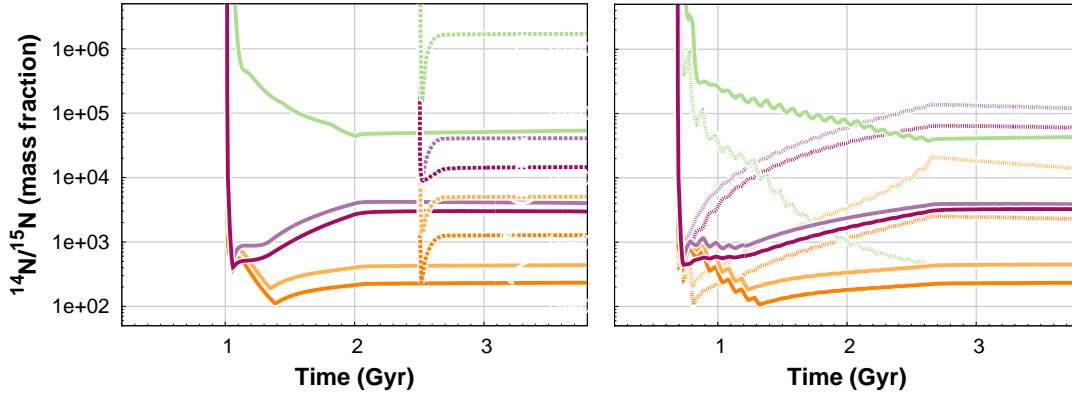


**Figure 9.** Behaviour of different CO isotope ratios in the interstellar medium for our model SMGs (see text).

**Table 2.** Final<sup>a</sup> abundance ratios of CNO isotopes in the interstellar medium for our grid of SMG models.

| Model  | SFH   | IMF       | $^{12}\text{C}/^{13}\text{C}$ | $^{14}\text{N}/^{15}\text{N}$ | $^{16}\text{O}/^{18}\text{O}$ | $^{18}\text{O}/^{17}\text{O}$ | $^{13}\text{C}/^{18}\text{O}$ |
|--------|---|-----------|-------------------------------|-------------------------------|-------------------------------|-------------------------------|-------------------------------|
| SMG-01 | Continuous, $\Delta t_{\text{burst}} = 1$ Gyr | Canonical | 118                           | $4.5 \times 10^4$             | $2.9 \times 10^3$             | 2.5                           | 6.2                           |
|        | One-shot, $\Delta t_{\text{burst}} = 20$ Myr  | Canonical | $1.7 \times 10^3$             | $1.8 \times 10^6$             | $3.9 \times 10^4$             | 5.3                           | 1.6                           |
|        | Gasping, $\Delta t_{\text{burst}} = 50$ Myr   | Canonical | 132                           | $3.8 \times 10^4$             | $2.3 \times 10^3$             | 2.4                           | 5                             |
|        | Gasping, $\Delta t_{\text{burst}} = 50$ Myr   | Top-heavy | 64                            | 453                           | 57                            | 3.2                           | 0.09                          |
| SMG-08 | Continuous, $\Delta t_{\text{burst}} = 1$ Gyr | Canonical | 162                           | 400                           | 79                            | 81                            | 0.2                           |
|        | One-shot, $\Delta t_{\text{burst}} = 20$ Myr  | Canonical | 765                           | $3.9 \times 10^3$             | 447                           | 126                           | 0.1                           |
|        | Gasping, $\Delta t_{\text{burst}} = 50$ Myr   | Canonical | 176                           | 424                           | 85                            | 65                            | 0.2                           |
|        | Gasping, $\Delta t_{\text{burst}} = 50$ Myr   | Top-heavy | 173                           | $1.7 \times 10^4$             | 334                           | 6                             | 0.9                           |
| SMG-09 | Continuous, $\Delta t_{\text{burst}} = 1$ Gyr | Canonical | 175                           | 214                           | 126                           | 45                            | 0.3                           |
|        | One-shot, $\Delta t_{\text{burst}} = 20$ Myr  | Canonical | 970                           | 695                           | 451                           | 99                            | 0.1                           |
|        | Gasping, $\Delta t_{\text{burst}} = 50$ Myr   | Canonical | 193                           | 220                           | 131                           | 37                            | 0.3                           |
|        | Gasping, $\Delta t_{\text{burst}} = 50$ Myr   | Top-heavy | 209                           | $2.4 \times 10^3$             | 480                           | 4                             | 1.1                           |
| SMG-11 | Continuous, $\Delta t_{\text{burst}} = 1$ Gyr | Canonical | 521                           | $2.7 \times 10^3$             | 344                           | 1.4                           | 0.23                          |
|        | One-shot, $\Delta t_{\text{burst}} = 20$ Myr  | Canonical | $1.3 \times 10^3$             | $1.3 \times 10^4$             | 819                           | 168                           | 0.13                          |
|        | Gasping, $\Delta t_{\text{burst}} = 50$ Myr   | Canonical | 546                           | $3.0 \times 10^3$             | 372                           | 1                             | 0.3                           |
|        | Gasping, $\Delta t_{\text{burst}} = 50$ Myr   | Top-heavy | 307                           | $6.3 \times 10^4$             | $2.8 \times 10^3$             | 0.01                          | 3.6                           |
| SMG-12 | Continuous, $\Delta t_{\text{burst}} = 1$ Gyr | Canonical | 184                           | $3.9 \times 10^3$             | 380                           | 27                            | 0.95                          |
|        | One-shot, $\Delta t_{\text{burst}} = 20$ Myr  | Canonical | $1.3 \times 10^3$             | $1.3 \times 10^4$             | 815                           | 168                           | 0.13                          |
|        | Gasping, $\Delta t_{\text{burst}} = 50$ Myr   | Canonical | 201                           | $3.7 \times 10^3$             | 419                           | 18                            | 1                             |
|        | Gasping, $\Delta t_{\text{burst}} = 50$ Myr   | Top-heavy | 232                           | $1.3 \times 10^5$             | $4 \times 10^3$               | 0.5                           | 7                             |

Note. <sup>a</sup>At star formation halt (see text).

**Figure 10.** As Fig. 9, for nitrogen.

model SMG-01, that does not include the effects of stellar rotation on the yields, always predicts  $^{13}\text{C}/^{18}\text{O} > 1$ , unless the IMF is skewed towards massive stars. The slope of  $x = 1.1$  assumed here for the top-heavy IMF in the high-mass domain is exaggerated – less extreme values would fit better the observations – but we prefer to show extreme variations, both for illustration purposes and to be consistent with the choice of Zhang et al. (2018). Alternatively, a ratio around unity could be reached if very high star formation rates, of the order of tens of thousands of solar masses per year, were assumed, which we deem unrealistic (see, however, Guarnieri et al. 2019, for a different perspective).

In the hot, turbulent medium of intense, gas-rich starburst galaxies forming stars at high redshifts, it may well be that the formation of fast rotators is favoured with respect to the local condi-

tions. For this reason, we compute models SMG-08 and SMG-09, in which all massive stars are supposed to rotate fast at birth, with  $v_{\text{rot}} = 300$  and  $150 \text{ km s}^{-1}$ , respectively, irrespective of their initial metallicity. In this case, a top-heavy IMF is needed once again to bring the predicted  $^{13}\text{C}/^{18}\text{O}$  ratio into agreement with the observations (see Fig. 9, lower panels, yellow and orange lines, and Table 2, last column).

As a last case study, we consider the possibility that massive stars are born fast rotators until a metallicity of  $[\text{Fe}/\text{H}] = -1$  is reached, above which the probability of gaining a high initial rotational velocity quickly drops to zero. This is exactly the picture that provides the best fit to the CNO data for the Milky Way (see Section 3.1). In this case, if a prolonged star formation (either bursty or continuous) is considered together with the yields of

Karakas (2010) and Doherty et al. (2014a,b) for LIMS and super-AGB stars, a ratio  $^{13}\text{C}/^{18}\text{O} \approx 1$  in SMGs can be obtained without any alteration of the IMF from its canonical form. If the yields of Ventura et al. (2013) are assumed in place of those by Karakas (2010) and Doherty et al. (2014a,b), or if a one-shot, short star formation event is assumed to build up the bulk of the stellar population, a  $^{13}\text{C}/^{18}\text{O}$  ratio approaching unity can be recovered, again, only by flattening the IMF in the high-mass domain (though, probably, a slope  $x = 1.1$  as adopted here is too much; see the entries referring to models SMG-11 and SMG-12 in Table 2, last column).

So in summary: When considering the effects of stellar rotation on the yields of massive stars, it is possible to explain a value of the ratio  $^{13}\text{C}/^{18}\text{O} \approx 1$  in SMGs without resorting to a top-heavy IMF only under very specific circumstances: (i) stars have to rotate fast only below a given metallicity threshold; (ii) the star formation must last long enough for a significant amount of  $^{13}\text{C}$  to be ejected by AGB stars; (iii) even in the latter case, the canonical IMF solution only holds for a particular choice of the AGB yield set. At star formation halt, in the case of a continuous star formation lasting 1 Gyr, LIMS and super-AGB stars have provided about 75 (model SMG-11) and more than 90 per cent (model SMG-12) of the total  $^{13}\text{C}$  content of the interstellar medium in our models. These percentages are higher than those reported with regard to the solar chemical composition in Section 3.1.3, pursuant to the more intense star formation activity characterizing the SMGs.

Clearly, observing different molecules to infer other isotope ratios is a crucial step towards a definite answer. In Table 2 we provide predictions, to be tested by future observations. In particular, from Table 2 it can be seen that simultaneous measurements of  $^{14}\text{N}/^{15}\text{N}$  and  $^{18}\text{O}/^{17}\text{O}$  isotope ratios would be particularly useful to break the degeneracies.

## 4 DISCUSSION

It is well known that stellar rotation significantly alters the outcome of stellar nucleosynthesis computations, especially so for the so-called spinstars, the first generations of extremely low-metallicity fast rotators in galaxies (Meynet & Maeder 2002; Chiappini et al. 2006; Ekström et al. 2008).

Recently, a large, homogeneous grid of massive star yields covering an extended range of initial masses, metallicities and rotational velocities has been published, including the contributions from the presupernova evolution, as well as from the final, explosive stages (Limongi & Chieffi 2018). The inclusion of these yields in GCE models, however, requires the adoption of a most uncertain quantity, the IDROV (Prantzos et al. 2018), similar in spirit to the stellar IMF, but by far more uncertain.

As pointed out by Penny & Gies (2009), as a matter of fact our ability to establish the true distribution of equatorial rotational velocities from direct observations of massive stars is severely hampered by the reduced sample sizes. One may hope to infer the Galactic IDROV indirectly, from a fit to the chemical properties of Galactic stars of different ages/metallicities. However, as stressed by Prantzos et al. (2018), this is a risky procedure, since different combinations of IDROVs and IMFs may provide equally good results. Moreover, the Galactic IDROV may not apply to other galaxies.

Indeed, Wolff et al. (2007) confirm that massive stars formed in high-density regions lack the numerous slow rotators seen for their counterparts born in low-density regions and the field, with the metallicity also likely playing a role (Meynet & Maeder 1997).

But alas, the most updated census of massive stars in the Galaxy and Magellanic Clouds does not show evidence for significant differences in early-type stellar rotational velocities with metallicity (Dufton et al. 2019, and references therein)!

Owing to all the above-mentioned uncertainties, we prefer to study some extreme cases here. We rather crudely assume that all stars rotate fast, or do not rotate at all or, in some cases, we consider the existence of a metallicity threshold determining an abrupt transition between these opposite regimes. We do not pretend to depict faithfully the complex reality of galaxies, but expect their true evolution to sit somewhere in between the extreme cases discussed in this paper.

## 5 CONCLUSIONS

In this paper, we discuss the results we find when implementing in our GCE code a new, large grid of yields for massive stars covering a wide range of initial masses and metallicities and including the effects of different stellar initial rotational velocities on the nucleosynthesis (Limongi & Chieffi 2018).

The grid is first tested against available CNO abundance data for stars and molecular gas in the solar neighbourhood and Milky Way disc and then used to model the evolution of CNO isotopes in the typical SMG. In our sample of four strongly-lensed SMGs seen by ALMA, the observations suggest extremely low  $^{13}\text{C}/^{18}\text{O}$  ratios, that are thought to arise from an excess of massive stars in starbursts (Zhang et al. 2018, see also Brown & Wilson 2019, for recent work on local analogs). The following key conclusions can be drawn:

(i) In qualitative agreement with the results of the study by Prantzos et al. (2018), that are based on an analysis of the chemical abundances of solar neighbourhood stars, we find that our model predictions for the Galaxy can be reconciled with the observations on the assumption that most stars rotate fast until a metallicity threshold is reached above which the majority of the stars have small or null rotational velocities; the value of this metallicity threshold happens to coincide with the one characterizing the end of the halo phase in our model.

(ii) If the formation of fast rotators is favoured in the hot, turbulent medium of dusty starburst galaxies at high redshifts irrespective of metallicity, a value around unity for the  $^{13}\text{C}/^{18}\text{O}$  ratio as observed in SMGs needs a top-heavy IMF in order to be explained.

(iii) If, instead, a metallicity threshold prevents the formation of massive fast rotators at relatively high metallicities, similarly to what is suggested for the Milky Way, it is possible to explain the low  $^{13}\text{C}/^{18}\text{O}$  ratios observed in SMGs with a universal IMF; however, in this case the star formation in SMGs must last long ( $\sim 1$  Gyr) and some special choice has to be made as for the yields of LIMS and super-AGB stars.

Overall, when the yields of rotating massive stars are included in GCE models, the issue of whether the IMF varies (becoming flatter) during the most violent starburst events in the universe appears unsettled, unless a long-lasting SFH (either gasping or continuous) can be definitely ruled out. A firm conclusion waits for the determination of other isotopic abundances from submillimeter observations, as well as for a better understanding of star formation in extreme environments. A comparison of the chemical properties of the oldest stars in massive local ellipticals with the predictions of the models involving different elements would also be extremely useful.

## ACKNOWLEDGEMENTS

We are deeply indebted to Padelis P. Papadopoulos for pointing out the need for a thorough investigation of the role of massive fast rotators in the turbulent media of submillimeter galaxies, as well as for many enlightening discussions. DR acknowledges funding from INAF PRIN-SKA “*Empowering SKA as a Probe of galaxy Evolution with HI (ESKAPE-HI)*” program 1.05.01.88.04 (PI L. K. Hunt). This work benefited from the International Space Science Institute (ISSI, Bern, CH) and the International Space Science Institute–Beijing (ISSI-BJ, Beijing, CN) thanks to the funding of the team “*Chemical abundances in the ISM: the litmus test of stellar IMF variations in galaxies across cosmic time*” (PIs D. Romano, Z.-Y. Zhang). The research shown here acknowledges use of the Hypatia Catalog Database, which was supported by NASA’s Nexus for Exoplanet System Science (NExSS) research coordination network and the Vanderbilt Initiative in Data-Intensive Astrophysics (VIDA).

## REFERENCES

- Adande G. R., Ziurys L. M., 2012, *ApJ*, **744**, 194
- Alexander R. D., Armitage P. J., Cuadra J., Begelman M. C., 2008, *ApJ*, **674**, 927
- Amarsi A. M., Nissen P. E., Asplund M., Lind K., Barklem P. S., 2019, *A&A*, **622**, L4
- Asplund M., Grevesse N., Sauval A. J., Scott P., 2009, *ARA&A*, **47**, 481
- Audouze J., Lequeux J., Vigroux L., 1975, *A&A*, **43**, 71
- Audouze J., Lequeux J., Rocca-Volmerange B., Vigroux L., 1977, in Audouze J., ed., *Astrophysics and Space Science Library* Vol. 67, CNO Isotopes in Astrophysics. pp 155–171
- Ayres T. R., Lyons J. R., Ludwig H.-G., Caffau E., Wedemeyer-Böhm S., 2013, *ApJ*, **765**, 46
- Barbuy B., 1983, *A&A*, **123**, 1
- Bath G. T., Shaviv G., 1978, *MNRAS*, **183**, 515
- Bertran de Lis S., Delgado Mena E., Adibekyan V. Z., Santos N. C., Sousa S. G., 2015, *A&A*, **576**, A89
- Boogert A. C. A., et al., 2000, *A&A*, **353**, 349
- Bradford C. M., et al., 2009, *ApJ*, **705**, 112
- Brown T., Wilson C. D., 2019, *ApJ*, **879**, 17
- Burbidge E. M., Burbidge G. R., Fowler W. A., Hoyle F., 1957, *Reviews of Modern Physics*, **29**, 547
- Carigi L., Peimbert M., Esteban C., García-Rojas J., 2005, *ApJ*, **623**, 213
- Cescutti G., Matteucci F., François P., Chiappini C., 2007, *A&A*, **462**, 943
- Chiappini C., Matteucci F., Gratton R., 1997, *ApJ*, **477**, 765
- Chiappini C., Matteucci F., Romano D., 2001, *ApJ*, **554**, 1044
- Chiappini C., Hirschi R., Meynet G., Ekström S., Maeder A., Matteucci F., 2006, *A&A*, **449**, L27
- Chiappini C., Ekström S., Meynet G., Hirschi R., Maeder A., Charbonnel C., 2008, *A&A*, **479**, L9
- Chin Y.-n., Henkel C., Langer N., Mauersberger R., 1999, *ApJ*, **512**, L143
- Colzi L., Fontani F., Rivilla V. M., Sánchez-Monge A., Testi L., Beltrán M. T., Caselli P., 2018, *MNRAS*, **478**, 3693
- Czekaj M. A., Robin A. C., Figueras F., Luri X., Haywood M., 2014, *A&A*, **564**, A102
- Dearborn D. S. P., Tinsley B. M., Schramm D. N., 1978, *ApJ*, **223**, 557
- Doherty C. L., Gil-Pons P., Lau H. H. B., Lattanzio J. C., Siess L., 2014a, *MNRAS*, **437**, 195
- Doherty C. L., Gil-Pons P., Lau H. H. B., Lattanzio J. C., Siess L., Campbell S. W., 2014b, *MNRAS*, **441**, 582
- Dufton P. L., Evans C. J., Hunter I., Lennon D. J., Schneider F. R. N., 2019, *A&A*, **626**, A50
- Edmunds M. G., Pagel B. E. J., 1978, *MNRAS*, **185**, 77P
- Ekström S., Meynet G., Chiappini C., Hirschi R., Maeder A., 2008, *A&A*, **489**, 685
- Fuhrmann K., 1998, *A&A*, **338**, 161
- Fuhrmann K., 2011, *MNRAS*, **414**, 2893
- Gratton R., Carretta E., Matteucci F., Sneden C., 1996, in Morrison H. L., Sarajedini A., eds, *Astronomical Society of the Pacific Conference Series* Vol. 92, Formation of the Galactic Halo...Inside and Out. p. 307
- Gratton R. G., Sneden C., Carretta E., Bragaglia A., 2000, *A&A*, **354**, 169
- Grisoni V., Matteucci F., Romano D., Fu X., 2019, arXiv e-prints,
- Guarnieri P., et al., 2019, *MNRAS*, **483**, 3060
- Gunawardhana M. L. P., et al., 2011, *MNRAS*, **415**, 1647
- Hedrosa R. P., Abia C., Busso M., Cristallo S., Domínguez I., Palmerini S., Plez B., Straniero O., 2013, *ApJ*, **768**, L11
- Henkel C., Mauersberger R., 1993, *A&A*, **274**, 730
- Henry R. B. C., Edmunds M. G., Köppen J., 2000, *ApJ*, **541**, 660
- Hinkel N. R., Timmes F. X., Young P. A., Pagano M. D., Turnbull M. C., 2014, *AJ*, **148**, 54
- Hughes G. L., Gibson B. K., Carigi L., Sánchez-Blázquez P., Chavez J. M., Lambert D. L., 2008, *MNRAS*, **390**, 1710
- Israelian G., Ecuivillon A., Rebolo R., García-López R., Bonifacio P., Molero P., 2004, *A&A*, **421**, 649
- Iwamoto K., Brachwitz F., Nomoto K., Kishimoto N., Umeda H., Hix W. R., Thielemann F.-K., 1999, *ApJS*, **125**, 439
- Jeřábková T., Hasani Zonoozi A., Kroupa P., Beccari G., Yan Z., Vazdekis A., Zhang Z.-Y., 2018, *A&A*, **620**, A39
- José J., Hernanz M., 2007, *Journal of Physics G Nuclear Physics*, **34**, R431
- Karakas A. I., 2010, *MNRAS*, **403**, 1413
- Kennicutt Jr. R. C., 1998, *ApJ*, **498**, 541
- Kobayashi C., Umeda H., Nomoto K., Tominaga N., Ohkubo T., 2006, *ApJ*, **653**, 1145
- Kobayashi C., Karakas A. I., Umeda H., 2011, *MNRAS*, **414**, 3231
- Kroupa P., 2002, in Grebel E. K., Brandner W., eds, *Astronomical Society of the Pacific Conference Series* Vol. 285, Modes of Star Formation and the Origin of Field Populations. p. 86 ([arXiv:astro-ph/0102155](https://arxiv.org/abs/astro-ph/0102155))
- Larson R. B., 1976, *MNRAS*, **176**, 31
- Lebzelter T., Straniero O., Hinkle K. H., Nowotny W., Aringer B., 2015, *A&A*, **578**, A33
- Lequeux J., Peimbert M., Rayo J. F., Serrano A., Torres-Peimbert S., 1979, *A&A*, **80**, 155
- Li H.-K., Zhang J.-S., Liu Z.-W., Lu D.-R., Wang M., Wang J., 2016, *Research in Astronomy and Astrophysics*, **16**, 47
- Limongi M., Chieffi A., 2018, *ApJS*, **237**, 13
- Lu J. R., Do T., Ghez A. M., Morris M. R., Yelda S., Matthews K., 2013, *ApJ*, **764**, 155
- Lucatello S., Tsangarides S., Beers T. C., Carretta E., Gratton R. G., Ryan S. G., 2005, *ApJ*, **625**, 825
- Maeder A., 1992, *A&A*, **264**, 105
- Marty B., Chaussidon M., Wiens R. C., Jurewicz A. J. G., Burnett D. S., 2011, *Science*, **332**, 1533
- Matteucci F., 1986, *MNRAS*, **221**, 911
- Matteucci F., D’Antona F., 1991, *A&A*, **247**, L37
- Matteucci F., François P., 1989, *MNRAS*, **239**, 885
- Matteucci F., Recchi S., 2001, *ApJ*, **558**, 351
- Matteucci F., Tosi M., 1985, *MNRAS*, **217**, 391
- Meynet G., Maeder A., 1997, *A&A*, **321**, 465
- Meynet G., Maeder A., 2002, *A&A*, **381**, L25
- Milam S. N., Savage C., Brewster M. A., Ziurys L. M., Wyckoff S., 2005, *ApJ*, **634**, 1126
- Mor R., Robin A. C., Figueras F., Lemasle B., 2017, *A&A*, **599**, A17
- Nayakshin S., Sunyaev R., 2005, *MNRAS*, **364**, L23
- Nissen P. E., Chen Y. Q., Carigi L., Schuster W. J., Zhao G., 2014, *A&A*, **568**, A25
- Nomoto K., Kobayashi C., Tominaga N., 2013, *ARA&A*, **51**, 457
- Paczynski B., 1998, *ApJ*, **494**, L45
- Papadopoulos P. P., 2010, *ApJ*, **720**, 226
- Papadopoulos P. P., Thi W.-F., Miniati F., Viti S., 2011, *MNRAS*, **414**, 1705
- Peimbert M., Torres-Peimbert S., Rayo J. F., 1978, *ApJ*, **220**, 516
- Penny L. R., Gies D. R., 2009, *ApJ*, **700**, 844
- Pignatari M., et al., 2015, *ApJ*, **808**, L43
- Polehampton E. T., Baluteau J.-P., Swinyard B. M., 2005, *A&A*, **437**, 957
- Prantzos N., Aubert O., Audouze J., 1996, *A&A*, **309**, 760

- Prantzos N., Abia C., Limongi M., Chieffi A., Cristallo S., 2018, *MNRAS*, **476**, 3432
- Roederer I. U., Preston G. W., Thompson I. B., Shectman S. A., Sneden C., Burley G. S., Kelson D. D., 2014, *AJ*, **147**, 136
- Romano D., Matteucci F., 2003, *MNRAS*, **342**, 185
- Romano D., Matteucci F., Molaro P., Bonifacio P., 1999, *A&A*, **352**, 117
- Romano D., Matteucci F., Salucci P., Chiappini C., 2000, *ApJ*, **539**, 235
- Romano D., Tosi M., Chiappini C., Matteucci F., 2006, *MNRAS*, **369**, 295
- Romano D., Karakas A. I., Tosi M., Matteucci F., 2010, *A&A*, **522**, A32
- Romano D., Matteucci F., Zhang Z.-Y., Papadopoulos P. P., Ivison R. J., 2017, *MNRAS*, **470**, 401
- Rybizki J., Just A., 2015, *MNRAS*, **447**, 3880
- Salpeter E. E., 1955, *ApJ*, **121**, 161
- Scalo J. M., 1986, *Fundamentals Cosmic Phys.*, **11**, 1
- Schmidt M., 1959, *ApJ*, **129**, 243
- Schmidt D. R., Woolf N. J., Zega T. J., Ziurys L. M., 2018, *Nature*, **564**, 378
- Schneider F. R. N., et al., 2018, *Science*, **359**, 69
- Smith H. E., 1975, *ApJ*, **199**, 591
- Sneden C., 1974, *ApJ*, **189**, 493
- Spite M., et al., 2005, *A&A*, **430**, 655
- Spite M., et al., 2006, *A&A*, **455**, 291
- Spitoni E., Romano D., Matteucci F., Ciotti L., 2015, *ApJ*, **802**, 129
- Suárez-Andrés L., Israelian G., González Hernández J. I., Adibekyan V. Z., Delgado Mena E., Santos N. C., Sousa S. G., 2016, *A&A*, **591**, A69
- Suda T., et al., 2008, *PASJ*, **60**, 1159
- Talbot R. J., Arnett D. W., 1974, *ApJ*, **190**, 605
- Toft S., et al., 2014, *ApJ*, **782**, 68
- Tosi M., 1982, *ApJ*, **254**, 699
- Truran J. W., Cameron A. G. W., 1971, *Ap&SS*, **14**, 179
- Umeda H., Nomoto K., 2002, *ApJ*, **565**, 385
- Ventura P., Di Criscienzo M., Carini R., D’Antona F., 2013, *MNRAS*, **431**, 3642
- Vigroux L., Audouze J., Lequeux J., 1976, *A&A*, **52**, 1
- Wielen R., Fuchs B., Dettbarn C., 1996, *A&A*, **314**, 438
- Wilson T. L., Rood R., 1994, *ARA&A*, **32**, 191
- Wolff S. C., Strom S. E., Dror D., Venn K., 2007, *AJ*, **133**, 1092
- Wouterloot J. G. A., Henkel C., Brand J., Davis G. R., 2008, *A&A*, **487**, 237
- Zhang Z.-Y., Romano D., Ivison R. J., Papadopoulos P. P., Matteucci F., 2018, *Nature*, **558**, 260